Textural evidence of fragmentation and densification processes in a fossilised shallow conduit on the flank of Nevados de Chillán Volcanic Complex

Flavia Rojas[1,2], John Browning[1,2*], Hugh Tuffen[3], José Cembrano[1,2], Javier Espinosa-Leal[1,2], Holly E. Unwin[4], Thomas M. Mitchell[5], Karin Hofer-Apostolidis[1,2], Philip G. Meredith[5]

[1] Department of Structural and Geotechnical Engineering, Pontificia Universidad Católica de Chile, Santiago, Chile.
[2] Centro de Excelencia en Geotermia de los Andes (CEGA), Chile.
[3] Lancaster Environment Centre, Lancaster University, Lancaster, UK.
[4] British Geological Survey, Keyworth, Nottingham, UK.
[5] Department of Earth Sciences, University College London, London, UK.

[*]Corresponding author: jbrowning@uc.cl

Highlights

- We report a shallow volcanic conduit on the SW flank of Nevados de Chillán.
- Textures within the conduit allowed us to define zones within the conduit.
- We performed an analysis of textures through a conduit perpendicular transect.
- This analysis revealed variable fragmentation and densification processes.

Abstract

Eruptive style transitions are common in silicic volcanoes and an improved understanding of transitional controls is necessary for hazard forecasting. Examples of hybrid eruptions where both explosive and effusive eruptive behaviours occur simultaneously have led to a re-examination of models used to understand these complex and poorly understood processes. Exposed fossilised conduits record evidence of magmatic processes and provide the opportunity to examine structures and textures related to these transitions. Here we present a conceptual model of the evolution of a narrow (2.5 m wide) conduit located on the SW flank of the Nevados de Chillán Volcanic Complex, Chile. This conduit records evidence of fragmentation and densification processes through intercalated and juxtaposed banded, porous and dense domains. To understand how the products of each eruptive style relate and evolve during conduit formation, we combined qualitative textural analyses at different scales (outcrop, optical microscope and electron microscope), pore size and shape measurements using ImageJ, connected porosity measurements made using a helium pycnometer and total water content measurements using Fourier transform infrared spectroscopy. The results allow us to identify five principal phases of the conduit evolution: (I) an explosive phase where the conduit is filled with pyroclastic material, evidenced in the

pyroclastic deposit preserved at the conduit wall, (II) a cyclic process of fragmentation and densification within the conduit that generates intercalation of the porous and dense domains, and leads to a hybrid explosive-effusive phase, (III) the formation of a dense magma plug that eventually seals the conduit and deforms vesicles and bands, (IV) the compaction of the pyroclastic domain due to the ascent of the plug, driving porosity reduction (to as little as 4% in the densest bands), with micro-folds and glassy fiamme, and (V) a final phase of post-sintering vesicle relaxation, yielding regular, mainly rounded, shapes. We compare our results with other exposed and examined conduits to propose a model of conduit evolution during small-volume, short-lived silicic eruptions.

Keywords: Volcanic conduit, fragmentation, densification, porosity, Nevados de Chillán

1. Introduction

Transitions between explosive and effusive eruption styles are common in eruptions of high-viscosity magmas at subduction-zone volcanoes (Preece et al., 2016), but the processes triggering them remain poorly understood (Melnik et al., 2005; Kendrick et al., 2013). Furthermore, recent silicic eruptions at the Chilean volcanoes Chaitén (2008-2009) and Puyehue-Cordón Caulle (2011-2012) have shown that these two styles can occur simultaneously, transitioning through a hybrid phase that can comprise the majority of the eruption duration (Schipper et al., 2013; Castro et al., 2014). These observations led to a re-evaluation of models explaining transitions based on changes in degassing systems from open to closed (e.g., Eichelberger et al., 1986; Jaupart and Allegre, 1991), as juxtaposed activity is inconsistent in suggesting that lava and pyroclasts are linked to a common degassing mechanism (Castro et al., 2014; Wadsworth et al., 2022).

The eruptive style is defined by a complex interplay of interrelated factors (Preece et al., 2016). In near-surface processes, i.e., in low-pressure environment (<10 km), these factors are associated with the growth of bubbles and crystals, which in turn have a major influence on magma porosity, permeability, viscosity, outgassing and fragmentation (Cassidy et al., 2018). Decompression generated in the magma as it rises causes volatiles to exsolve into bubbles as their solubility decreases with decreasing pressure (Sparks, 1978). This exsolution of bubbles, in turn, increases magma buoyancy further driving the ascent of the magma through the conduit (Nguyen et al., 2014). When ascent is slow gases can escape from the magma laterally or vertically through fractures, permeable walls or interconnected bubbles, generating effusive eruptions (Preece et al., 2016). In contrast, when the magma rises rapidly and overpressure is generated, bubbles grow and collapse, fragmenting magma and leading to explosive eruptions (Gonnermann and Manga, 2007).

It is the eruptive style that defines the types of hazards each volcano possesses (Cassidy et al., 2018). Explosive eruptive style is the most powerful and destructive type of volcanic activity (Papale, 1999). Its principal associated hazards are pyroclastic density currents (PDC) and tephra falls, which can cover thousands of square kilometres around the volcano (Wilson et al., 2014). By contrast, effusive eruptive style is related to less dangerous and more localized hazards. The most common being lava flows, which can vary considerably in their rates of transport velocity, between 10^{-5} and >5 m/s (Diniega et al., 2013). Transitions in eruptive style then require a change in risk mitigation plans and may even exacerbate associated hazards by deviating from "typical" and expected behaviour (Brett et al., 2020).

Different mechanisms have been proposed to explain eruptive style transitions, in addition to the classical models of changes in the degassing regime between open and closed. These include changes in the permeability and porosity of the system due to tuffisite generation (e.g., Stasiuk et al., 1996), sintering (e.g., Vasseur et al., 2013; Wadsworth, 2020) or both (e.g., Castro et al., 2014; Saubin et al., 2016; Heap et al., 2019; Schipper et al., 2021; Trafton and Giachetti, 2022; Unwin et al., 2023), magma degassing due to fault slip (e.g., Novoa et al., 2022) or a change in magma ascent rate (e.g., Woods and Koyaguchi, 1994; Burgisser and Gardner, 2004). These different processes are recorded in the texture of the volcanic products, providing important information on the dynamics of the eruption and allowing the reconstruction of eruptive histories (Cashman et al., 1994). For example, gas loss and bubble growth are recorded in the porosity and permeability of rocks (Shea et al., 2010), tuffisites represent degassing processes through fractures (Heiken et al., 1988), different degrees of crystallinity are related to different rates of magma ascent and decompression (Wright et al., 2012) and vesicle shape and morphology are related to the evolution of the eruptions (Alfano et al., 2012).

The textures associated with eruption styles and their transitions have been extensively studied in eruption-related products, but much less so in volcanic conduits, as exposed and well-preserved conduits are scarce (Stasiuk, 1996; Tuffen and Dingwell, 2005; Soriano et al., 2006; Unwin et al., 2023). This work presents a textural study of a fossilised volcanic conduit located on the west flank of the Nevados de Chillán Volcanic Complex. The conduit records evidence of interactions between processes associated with both explosive and effusive eruptive behaviour, providing an opportunity to examine structures and textures related to eruptive style transitions. Specifically, we analyse variations in porosity, water content, pore size and shape distribution, comparing textures from the different lithological domains. The results obtained lead to a conceptual model of conduit evolution that can be applied to other conduits with similar characteristics leading to an enhanced understanding of eruption transition mechanics.

2. Geological context and case study

The Nevados de Chillán Volcanic Complex (NCVC) is located in the Chilean Southern Volcanic Zone (36°52′S; 71°23′W; 3212 m.a.s.l). The zone is characterised by a slightly dextral-oblique convergence between the Nazca and South American plates at a rate of 7-9 cm/yr. that has prevailed during the last 20 Ma (Stern, 2004; Cembrano and Lara, 2009). The NCVC is one of the most dangerous volcanoes in Chile, ranked fourth in terms of hazards and risk by the Chilean Geological Survey (Oyarzún et al., 2022). The active crater is very close to population and tourist centres (<5 km) and more than 4000 people live within its zone of influence, a number that increases significantly in winter because of the ski centre located on the west flank (Cardona et al., 2021). In addition, Holocene activity has been characterised by pyroclastic flows and lahars (Dixon et al., 1999; Moussallam et al., 2018), which are among the most dangerous hazards.

The NCVC is divided into two main sub-complexes: Cerro Blanco (NW) and Las Termas (SE), separated by about 6 km (Dixon et al., 1999). There are 13 eruptive centres are aligned along a NW trend and extending along a 10 km-long ridge. This trend appears to be related to a regional structure of the basement, the Chillán-Cortaderas lineament (Naranjo et al., 2008; Stanton-Yonge et al., 2016). Two satellite cones, Parador and Lagunillas, have also been geochemically associated with the complex (Fig. 1a). The compositional range of the complex varies between basaltic andesites (53% SiO2) and low-silica rhyolites (71% SiO2), and the geology is characterised by volcanic sequences alternating between subglacial and subaerial products (Dixon et al., 1999). The basement of the complex is composed of the Cura-Mallín and Cola de Zorro formations. The Cura-Mallín Formation is a folded sequence of volcano-sedimentary rocks that have been dated to the Lower-Middle Miocene. This latter unit is discordantly overlain by the Upper Pliocene-Pleistocene Cola de Zorro Formation, a sequence of sub-horizontal volcanic rocks. This unit is intruded by Miocene intrusive rocks of the Santa Gertrudis-Bullileo batholith (Naranjo et al., 2008; Benet et al., 2021; Cardona et al., 2021).

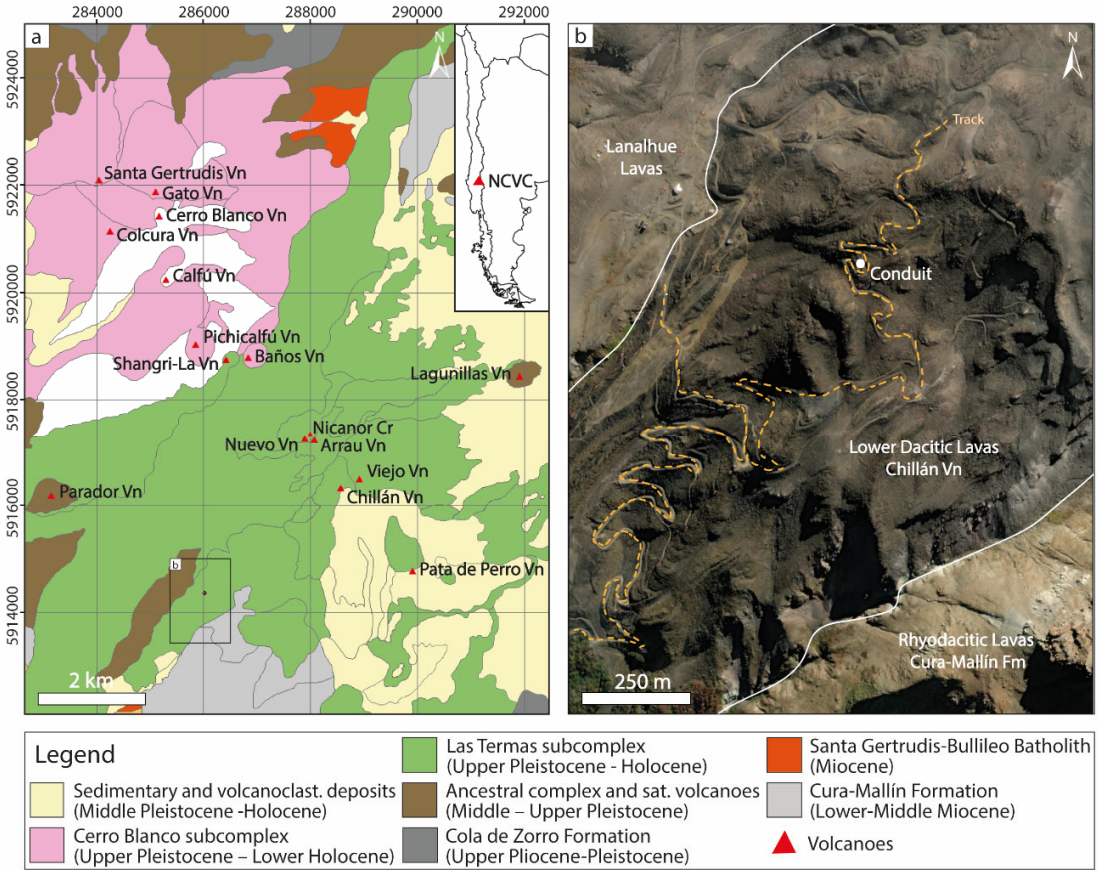

Figure 1: Location and geological setting of the Nevados de Chillán Volcanic Complex and the exposed conduit. **a)** Geological map showing the main units, formations, and eruptive centres of the NCVC, modified from Naranjo et al. (2008). The inset shows the location of the NCVC within Chile. **b)** Map view showing the location of the exposed conduit and the surrounding lithologies. Map imagery: Esri, Maxar and Earthstar Geographics, and the GIS User Community.

The NCVC has a long history of eruptions, its first activity occurring at 640 ka, with the eruption of an extensive andesitic lava flow (Dixon et al., 1999). The most important recorded historical eruptions occurred in 1906-1948, 1973-1986, 2003 and 2008. The 2008 eruption was succeeded by the most recent eruptive period that began in January 2016. During the last century, volcanic activity has been concentrated in the Las Termas sub-complex, with mainly dacitic products (Cardona et al., 2021; Oyarzún et al., 2022). The NCVC has been characterised by variations of explosive and effusive eruptive behaviour, including the last cycle. The first eruption in January 2016 produced a 2km-high ash plume and subsequent eruptions had similar characteristics, eroding the surface of the Arrau cone, and eventually converging to create the new Nicanor crater (Fig. 1a). A dacitic lava dome was then extruded and collapsed within the same crater, generating the effusion of four lava flows (Cardona et

al., 2021). After months without seismic or eruptive activity, the Chilean Geological Survey lowered the NCVC alert, ending this eruptive period in January 2023 (Sernageomin, 2023).

The studied conduit is located on the SW flank (36°53'S; 71°24'W; 2294 m.a.s.l) of the Chillán volcano, a dacitic cone composed mainly of lava intercalations and pyroclasts within the Las Termas subcomplex (Fig. 1b; Moussallam et al., 2018). The conduit is part of a unit called the Lower Dacitic Lavas, characterised as crystal-poor silica-rich dacites with blocks up to 1 m across, often interstratified with reworked ash and pumice deposits of uncertain age (Naranjo et al., 2008), but according to stratigraphic correlations, they are possibly younger than 2.27 ka (Dixon et al., 1999). The 2.5 m-wide, 3 m-high, and 3 m-long outcrop records three main lithological domains and has contacts with the wall rock exposed (Fig. 2). The western part of the conduit forms a yellowish domain dominated by apparently porous material with pyroclastic textures. The centre is a grey domain, formed by a lava-like, fractured and apparently dense material. Finally, the reddish domain in the eastern area is formed by a brecciated and oxidised material.

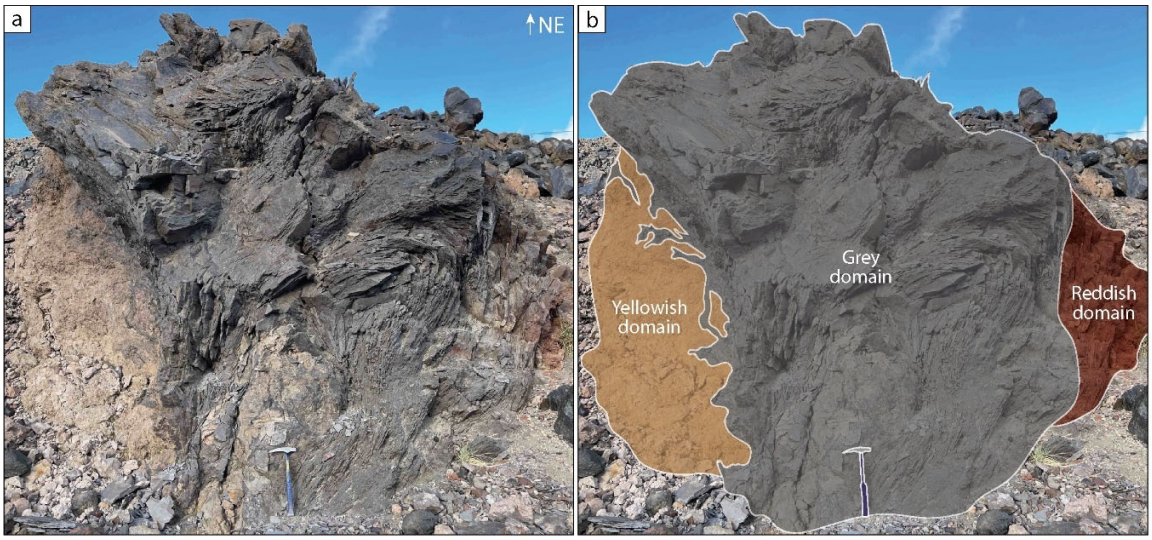

Figure 2: Picture and delimitation of conduit domains. Geological hammer as a scale (40 cm). **a)** Picture of the 2.5 m-wide, 3 m-high, 3 m-long exposed conduit. **b)** Annotated image indicates the principal domains by colour**:** the western yellowish domain, the central grey domain, and the eastern reddish domain.

3. Methods

3.1. Fieldwork

The outcrop was divided into seven zones (designated Z1 to Z7), based on observable differences in colour, texture and fracture type. Z1 corresponds to the yellowish lithological domain, Z2 mostly to the yellowish domain but in contact with the grey lithological domain

structures, Z3-Z6 correspond to the grey domain but are separated due to different degrees of fracturing and Z7 corresponds to the reddish lithological domain in contact with the grey domain structures. Each zone is described in detail in section 4.1 below, including its dimensions and lithological characteristics, comprising mineralogy, macrotextures and grain and pore sizes. One sample, approximately 15x10x10 cm, was taken from each zone and used for a multiscale analysis involving petrographic descriptions, thin sections analysis and laboratory measurements of physical properties. High-resolution photographs and videos were taken in-situ in the field with cameras and drones. These images were used to provide a complete representation of the outcrop and generate a 3D model using structure-from-motion techniques (James et al., 2017) and the software AGISOFT (Bistacchi et al., 2022).

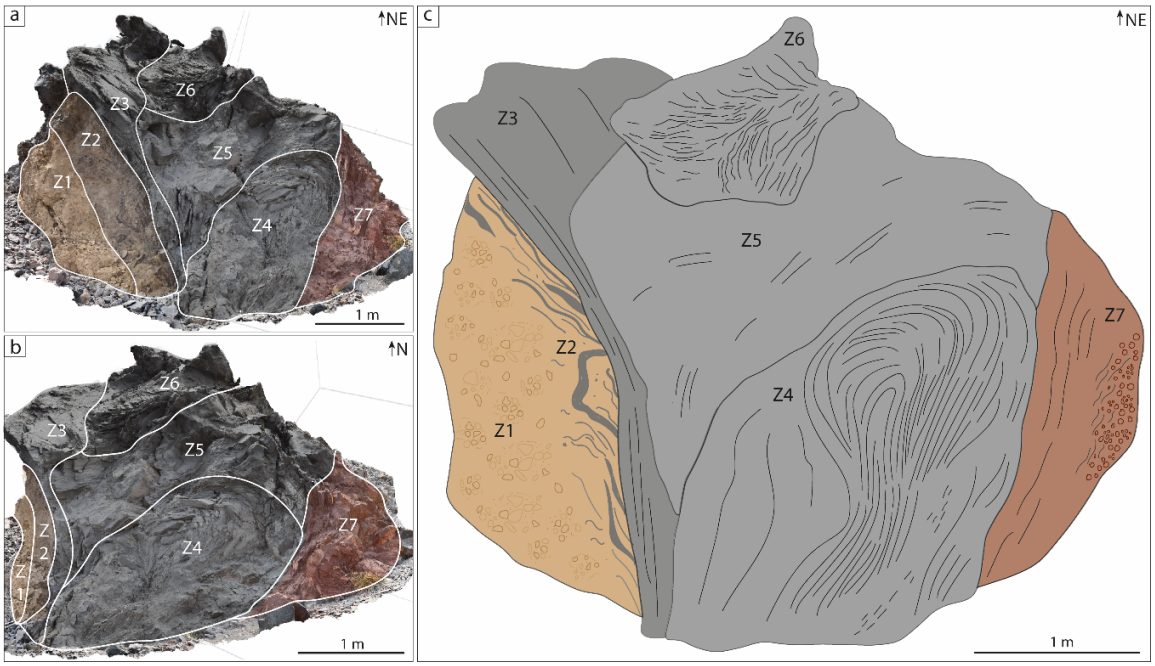

Figure 3: Three-dimensional structure-from-motion model of the exposed conduit in two orientations. Superimposed on the images are seven zones classified by detailed textural observation. **a)** facing NE and **b)** facing N, showing all the zones. **c)** Sketch of the exposed conduit with the seven zones established.

3.2. Textural descriptions at different scales

The seven hand specimens collected from each zone were described with the aid of a hand lens. Ten polished thin sections were prepared from the seven samples, one per zone from Z1, Z3, Z4, Z5 and Z6, but three from Z2 and two from Z7, as the last two were the inter-domain contact zones and therefore of greatest interest. All the thin sections were described petrologically and texturally using a petrographic microscope with transmitted and reflected light. Between 10 to 15 photographs were taken of each thin section, using the different lenses

and modes of the microscope in order to capture the most important textural aspects of each zone. Samples from representative zones of each of the three main domains (Fig. 2b) and their contacts (Z1, Z2, Z4 and Z7) were selected for scanning electron microscope (SEM) analysis. The SEM thin sections were coated with carbon, and images for textural description were taken at a range of magnifications between 100x and 4000x using the FEI Quanta 250 SEM at the University of Chile and the Jeol JSM-7800F FEG SEM at Lancaster University. Qualitative descriptions of pore and crystal shapes and distributions, microstructures and volcanic textures were made for all scales.

3.3. Quantitative textural analysis

Four 1800x magnification SEM images for quantitative textural analysis were taken at representative locations of each domain in the selected thin sections (Z1, Z2, Z4 and Z7), providing a total of 24 images. The high-resolution images were processed using the free Java-based software ImageJ to obtain size distribution and shape parameters of pores (Schneider et al., 2012). The shape parameters were obtained directly from ImageJ processing and include area, major and minor axis, aspect ratio and solidity factor. The aspect ratio (width/length) is related to the elongation of the pores. The solidity factor is the ratio between the area of the pore and the area of the convex hull, which is in turn the line of shortest distance between the maximum projections on a pore outline and can be related to the roughness of individual pores (Alfano et al., 2012). Due to the low contrast between the solid phase and the pores in the greyscale SEM images, the pores were hand-drawn in Adobe Illustrator from each image to obtain accurate measurements. All pores that could be delineated were drawn. The size distribution plots were made with the value of the major axis of the pores.

3.4. Porosity measurements

Porosity was determined using two different methods: 2D porosity calculations from SEM images using ImageJ, and direct measurements using a Micrometrics AccuPyc II 1340 Helium pycnometer at University College London. In the first method, the same 24 images prepared for the quantitative textural analysis were used, but the void space was identified with ImageJ's automatic threshold. This automatic filter allows differentiation of the information from all the shapes of interest (the pores) in black, and the background (the solid phase) in grey (Hu et al., 2023). The total area of the image is first determined, and then the total area occupied by pores is summed. The 2D porosity is then calculated as the ratio between these two areas, and representative values for each domain are obtained simply by averaging these porosity values. For the second method, one representative sample per main domain was selected from Z1, Z4 and Z7. Connected porosity is calculated from the difference between the bulk volume of the sample and the volume of the solid matrix that is measured by the pycnometer, using the equation: $\phi = (V_{bulk} - V_{measured}) \,/\, V_{bulk}$

(Columbu et al., 2021). This method usually uses cylindrical core samples, so that the bulk volume can be calculated simply from the equation for the volume of a cylinder ($\pi r^2 h$). However, our conduit samples had irregular shapes and could not be cored, so it was necessary to use an alternative method. In this method, the raw, irregular sample is weighed (M_{raw}), and an initial measurement of the volume of the solid matrix (V_{raw}) is made in the pycnometer. The sample is then removed from the pycnometer and covered with paraffin wax of known and calibrated density (ρ_{wax}). This is done by melting the wax on a hot plate until it is liquid and then dipping the sample into the wax a few times until it is completely coated. The coated sample is then re-weighed (M_{wax}) and reintroduced into the pycnometer to measure its total volume (V_{wax}). The layer of wax acts as a sealant, and prevents gas entering the sample pore space, thus allowing the bulk volume of the sample (V_{bulk}) to be calculated from the equation: $V_{bulk} = V_{wax} - (M_{wax} - M_{raw}) / \rho_{wax}$.

3.5. Fourier Transform Infra-red Spectroscopy

Fourier Transform Infra-red (FTIR) spectroscopy was used to obtain the dissolved magmatic water content of Z1, Z2 and Z3, with the aim of analysing changes in this transition between the yellow domain, the contact area and the beginning of the central grey domain. This is a practical and well-documented method of obtaining measurements of H and C species in volcanic glasses (von Aulock et al., 2014), based on the frequency and intensity at which chemical bonds vibrate when subjected to infrared radiation from the electromagnetic spectrum passing through or reflecting off an object of interest (Wysoczanski and Tani, 2006). This method has two modes of use: transmission and reflection, each with different objectives. In the transmission mode, the sample is placed in the path of the IR beam and the resulting transmitted IR signal is recorded and used to make a concentration determination (Chen et al., 2015). The reflection mode, in this case, was used to obtain the thickness of the samples and is highly accurate because it depends on the position of the wavenumber. The thickness measurement is based on the principle that the wavelength of the interference fringe pattern is directly proportional to the thickness and refractive index of the sample (Nishikida et al., 1996). Thus, the thickness corresponds to the number of waves in any wavenumber interval, in the relation $\partial = m/2n(v1 - v2)$, where m is the number of waves in a selected wavenumber range, n is the refractive index of the sample, and v1 and v2 are the highest and lowest wavenumbers over the selected interval (Wysoczanski and Tani, 2006).

Sample preparation is crucial for the proper functioning of this method, with the sample comprising a double-polished wafer approximately 50-200 μm thick. One wafer per zone was prepared and analysed at Lancaster University using a Thermo Nicolet IR interferometer. Three transects with 10 measuring points each were carried out in the Z1 wafer, in wafer Z2 one transect with 18 measuring points and in wafer Z3 three transects with 11 measuring points each. At each measurement point transmission spectra and reflection spectra were obtained, to quantify sample thickness and absorption peak heights. OMNIC software was

used to process the data. First, the reflection spectra were used to determine the wavelength and the thickness calculation. Then, the transmission data were corrected with a manual baseline and, for each spectrum, the peak height around wavenumber 3500 was searched, as it is this peak that is commonly used to calculate total H_2O concentrations (Chen et al., 2015). Then, total water concentration values are calculated using the Beer-Lambert Law following the procedure described in von Aulock et al. (2014). The error in the measurements is also calculated, corresponding to 10%, associated with uncertainty in the calculation of thickness, absorption coefficients, absorption peak measurements, generalisations in the density of the samples and calibration of the equipment (von Aulock et al., 2014; Chen et al., 2015; Saubin et al., 2016).

4. Results

4.1. Qualitative textural analysis

The studied outcrop represents a volcanic conduit, exposed to a height of around 3 m, with a fan-like shape in section and lateral textural variations (Fig. 3). We interpret the outcrop as a conduit (e.g., Tuffen and Dingwell 2005) rather than near-flow surface facies of a subaerial lava flow (e.g., Farquharson et al. 2022) because of the near-vertical walled but flaring morphology, the lithological contrast between the breccias at the walls, the suite of textures that share many similarities, albeit on an order of magnitude smaller scale, to those recently documented in the Mule Creek silicic conduit (Unwin et al. 2023), and the orientation of the inferred conduit walls, which correspond with both regional and local tectonic features (Lupi et al., 2020). The central part of the conduit is composed of a massive and fractured grey domain in contact with a poorly consolidated banded yellowish unit to the NW, and with a consolidated reddish unit to the SE that is also banded but with fewer, wider bands. The fan-shaped central grey domain varies in width from 1.2 m at the lowest part to 2.5 m at the uppermost part. The contact plane between Z2 and Z3 has an NE orientation and dips sub-vertically, but the inner bands in Z2 rotate internally and dip at different angles. The seven textural zones of the conduit, defined by field observations (Fig. 3), are described below.

Zone 1 (Z1)

Zone 1 represents the exposed western extent of the poorly-consolidated, yellowish domain which has a thickness of between 35 and 65 cm. The unit corresponds to a polymictic lithic tuff, with both juvenile and glassy clasts from <1 mm up to 20 cm, but predominantly between 1 to 2 cm (Fig. 4a). The matrix consists of very fine-grained mineral fragments with only 0.05-0.3 mm plagioclase observable in optical microscope images (Fig. 4b). Other minerals, such as amphibole, clinopyroxene and opaque minerals related to alteration are also recognised via optical microscopy. SEM images reveal rounded, small (0.5-3 μm) pores, but larger pores tend to have more irregular edges and elongation. Pores with curved polygonal

(horseshoe) shapes and microcracks are also present. Coupled particles are observed, in some cases forming "necks" at the particle interfaces (Fig. 4c).

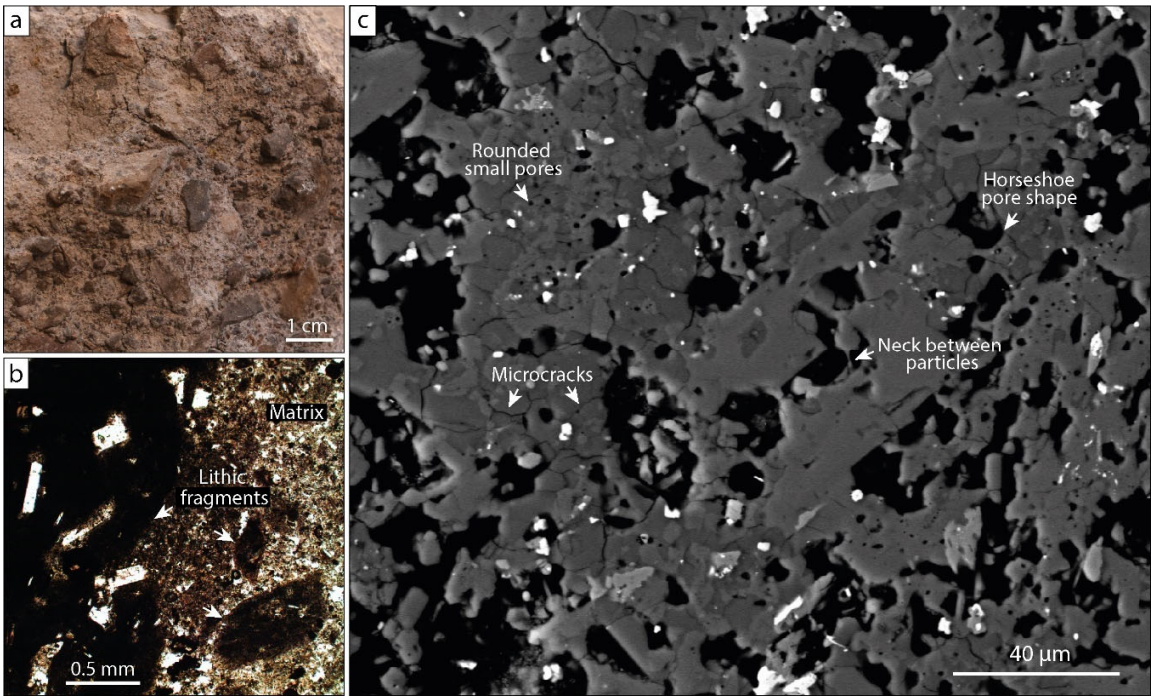

Figure 4: Textural aspects of Zone 1. **a)** Hand specimen, showing the matrix and poorly consolidated clasts of different textures and colours. **b)** Thin-section image showing polymictic lithic fragments and the fine-grained matrix. **c)** SEM image showing examples of microcracks, neck formation between neighbouring particles and horseshoe-shaped pores.

Zone 2 (Z2)

Zone 2 corresponds to an area of transition and interaction between Z1 and Z3, which varies in width between around 63 and 76 cm. This zone exhibits two distinct textures and colours. Parts are essentially identical to Z1, being a poorly-consolidated yellowish tuff unit, but are juxtaposed and intercalated with a series of grey bands ~0.2 mm-10 cm in width. To differentiate these two domains within Z2, we use the notation Z2y to indicate the yellowish tuff unit and Z2g to indicate the denser grey unit. The bands are mostly elongated, wavy and sub-parallel to the main contact plane between Z2 and Z3. Some of the bands cross the entire length of the exposed height of the conduit (Fig. 5a). At the hand specimen scale (Fig. 5b), it is possible to observe the intertwining of the two domains, Z2y and Z2g, with highly irregular thin bands forming micro-folds and dark-reddish reaction edges on their contacts.

Figure 5d shows a representative example of the contact between Z2y and Z2g at the microscopic scale. In this image, the contacts are highly sinuous and some of the bands appear to protrude into one another often forming sharp pointed terminations. The grey bands have a porphyritic texture, with a vitreous matrix and euhedral and fragmental 0.05-1 mm

plagioclase crystals. Eutaxitic textures are also observed, with glassy, elongated 0.1-20 mm long fiamme (Fig. 5e). The inter-band interaction zones show a reddish alteration and devitrification textures with clusters of fibrous microcrystals, in some cases with near-circular cross sections indicative of spherulitic intergrowths (e.g., Castro et al., 2008; Fig. 5f). High-magnification SEM images show how the porosity (void space shown in black) varies between the bands of the two domains and how they interleave (Fig. 5c). In Z2y, the pores vary over a wide range of sizes and, as their size increases, they become more irregular and have more concavities. The pores in Z2g are mostly only a few μm in size and rounded. In some areas, rounded and globule-like glassy clasts that are inferred to have welded onto the crystal surfaces and crystal interfaces show the same neck formation as in Z1, see further information in the discussion section.

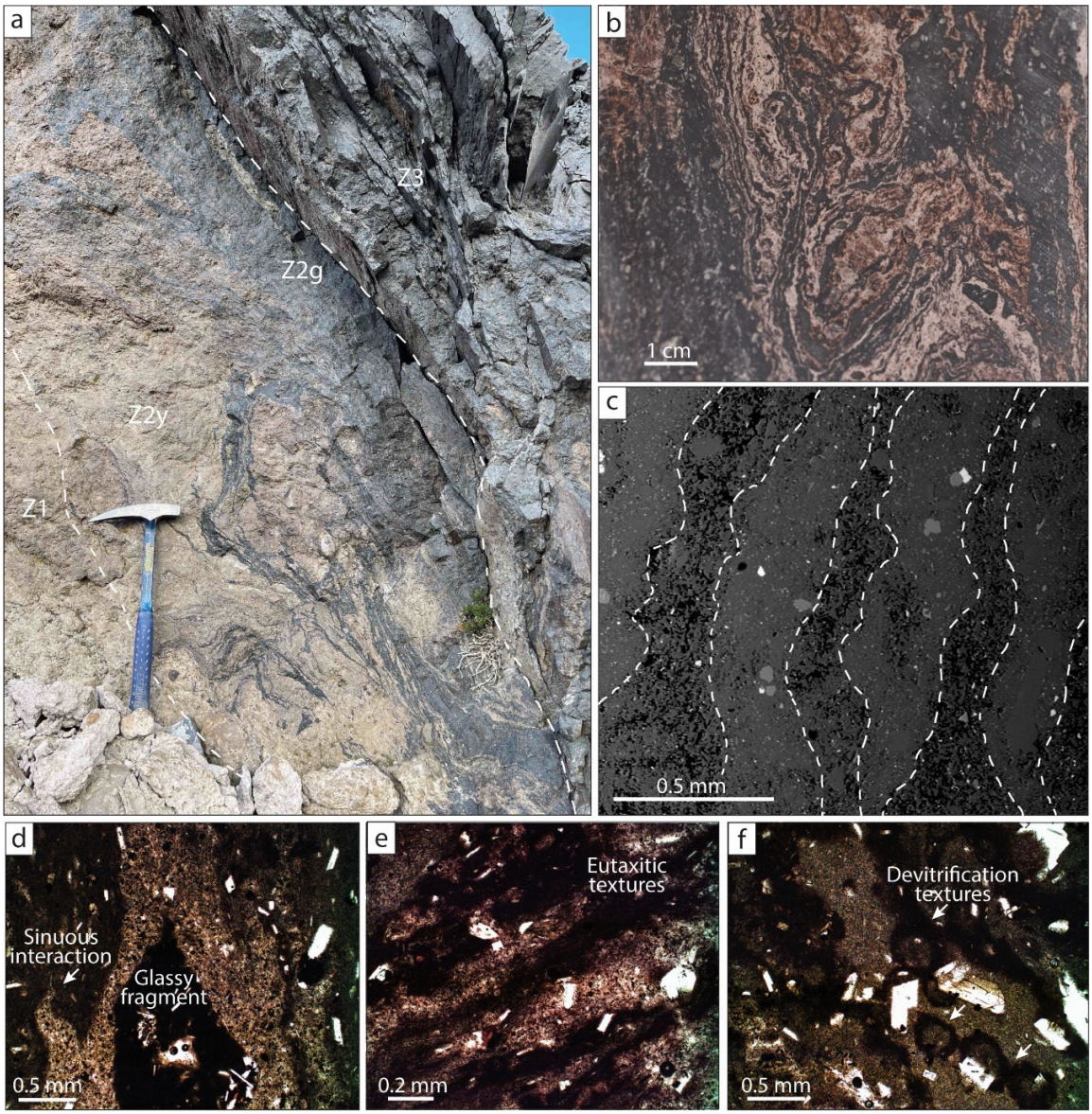

Figure 5: Textural aspects of Zone 2. **a)** Z2 in the outcrop, the white segmented lines represent the zone boundaries. Geological hammer as scale (40 cm). Close juxtaposition of grey (Z2g) and yellow domain (Z2y) bands is evident. **b)** Saw-cut flat surface of the hand specimen. The thin folded bands with inferred red and oxidised reaction edges at the contacts are visible. **c)** SEM image at 200x magnification, showing the different porosities (in black) of the two domains and how the bands are interleaved. **d-f)** Optical microscope images showing relevant textural features such as sinuous contacts, eutaxitic bands and zones of alteration and devitrification.

Zone 3 (Z3)

Zone 3 occurs to the east of the contact plane between the yellow and grey domains (Fig. 6a) and is 8-18 cm wide. Z3, therefore lies within the grey domain, but some thin (~5 mm) bands that constitute the yellow domain are still present (Fig. 6b). Mineralogy is dominated by 0.05-1 mm plagioclase crystals, which are oriented preferentially. Amphibole and clinopyroxene are also present in smaller proportions. This zone has two types of fractures, some sub-parallel to the contact plane and others perpendicular to the bands of yellow domain material. Sub-parallel fractures have ~2-3 cm spacing and aperture of 0.2-0.5 mm (Fig. 6c), whereas those perpendicular to the bands are more closely spaced (every 0.1-1 mm) with an average opening of 0.3 mm (Fig. 6d). Distinction between Z3 and the rest of the grey domain zones is evident from difference in colour and fracture density, with Z3 being darker and less fractured.

Zone 4 (Z4)

Zone 4 corresponds to the central part of the grey domain and is 42-85 cm wide, and ~170 cm high (Fig. 6e). Its main characteristic is the presence of inclined and tightly folded layers with fractures marking the boundaries of the individual folds. The unit has a glomeroporphyritic texture (Fig. 6f), with clusters of plagioclases and clinopyroxene crystals (Fig. 6h) and a matrix with 0.05-0.5 mm plagioclase crystals (Fig. 6g). SEM images show 0.2-8.4 μm diameter pores and the largest quantity of microlites (>60% vol) of all zones, which are 5-20 μm in length.

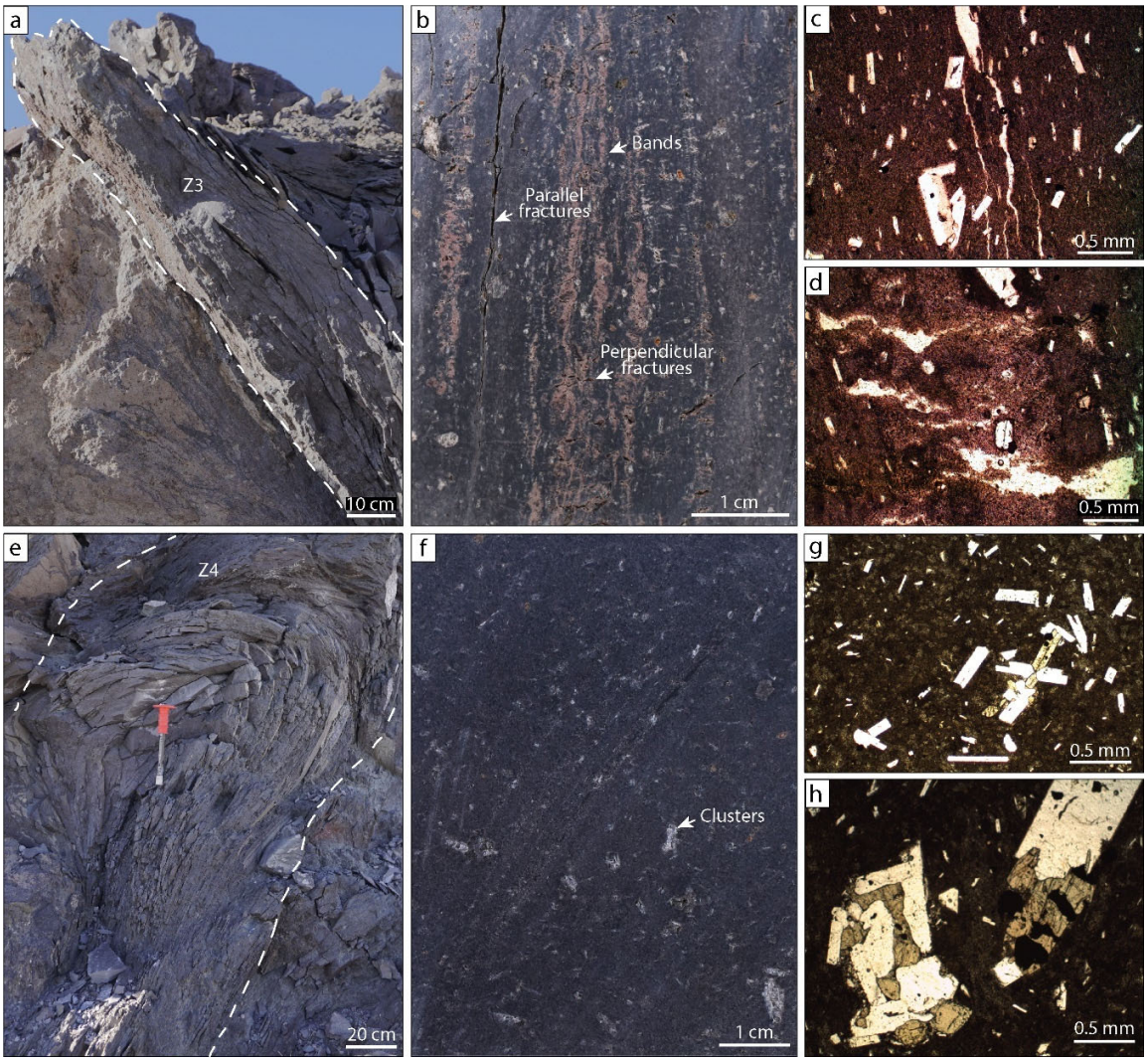

Figure 6: Textural aspects of Zone 3 and Zone 4. **a)** Part of Z3 in the outcrop, with boundaries delimited by white segmented line. **b)** Saw-cut flat surface of hand specimen of Zone 3 showing remnant bands of the yellowish domain material and fractures parallel and perpendicular to them. **c-d)** Thin section images of Zone 3 in plane-polarised light, showing the two types of fractures. **e)** Part of Zone 4 in the outcrop, with boundaries delimited by the white segmented line. **f)** Saw-cut flat surface of hand specimen of Zone 4 showing the glomeroporphyritic texture. **g-h)** Thin section images of Zone 4 under the microscope, showing the matrix and examples of the cluster of plagioclases and clinopyroxene.

Zone 5 (Z5)

Zone 5 is located above Z4, and we classify it as part of the grey domain; its exposure is ~180 cm wide and 65-74 cm high. It comprises the most homogeneous material within the conduit, being uniform in colour, with little observable porosity at the hand specimen scale and presenting only isolated fractures in specific areas. The zone has a glomeroporphyritic texture presenting a high abundance of clusters of plagioclase and clinopyroxene microcrystals (Fig. 7d). The matrix is mainly glass and plagioclase with individual oriented crystals with lengths varying between 0.05-0.3 mm (Fig. 7e).

Zone 6 (Z6)

Zone 6 is above Z5 (Fig. 7a) and ~120 cm wide by 70 cm high. We classify it as part of the grey domain, and it is the zone with the highest density of fractures in the conduit, with ~1-2 cm spacing. It presents a glomeroporphyritic texture, like Z5, but with a lower proportion of crystal clusters and phenocrysts (Fig. 7b). Interstitial, star-shaped domains of the same yellow pyroclastic material between devitrified patches are also present (Fig. 7c).

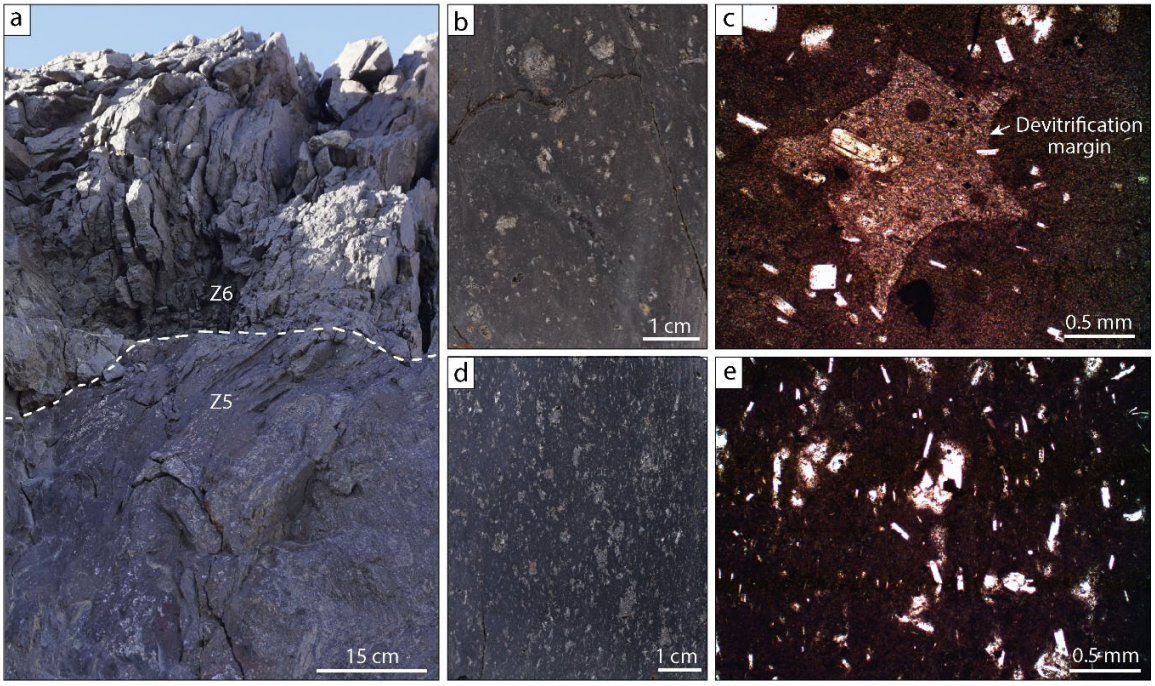

Figure 7: Textural aspects of Zone 5 and Zone 6. **a)** Part of both zones in the outcrop, shows their arrangement and the differences in the degree of fracturing. **b)** Saw-cut flat surface of hand specimen of Z6 showing the glomeroporphyritic texture. **c)** Thin section images of Z6 under the microscope, showing a star-shaped domain of crystal-rich groundmass between devitrified patches. **d)** Saw-cut flat surface of hand specimen of Z5 showing the glomeroporphyritic texture, with more clusters than Z6. **e)** Thin section images of Z5 under the microscope, showing the glassy matrix with 0.05-0.3 mm plagioclases preferentially oriented.

441 **Zone 7 (Z7)**

442 Zone 7 corresponds to the contact area between the grey (Z7g) and the reddish (Z7r) domain,
443 at the eastern margin of the conduit. Only 25 cm of its ~70 cm width, corresponds to the
444 outcrop of the reddish domain. Zone 7 represents an interaction zone, like Z2, but is much
445 narrower, being no more than 8 cm wide. The grey domain contains 0.2-0.5 mm wide
446 elongated bands that are wavy and sub-parallel to the main contact. Z7g has a porphyritic
447 texture, with a vitreous matrix and euhedral and fragmental plagioclase phenocrysts, ranging
448 from 0.05-0.3 mm in length. Inter-band contacts show reddish alteration and devitrification
449 textures with fibrous microcrystals. Z7r has a similar texture to Z1, but with 0.2-10 μm pores
450 and a reddish colour.
451

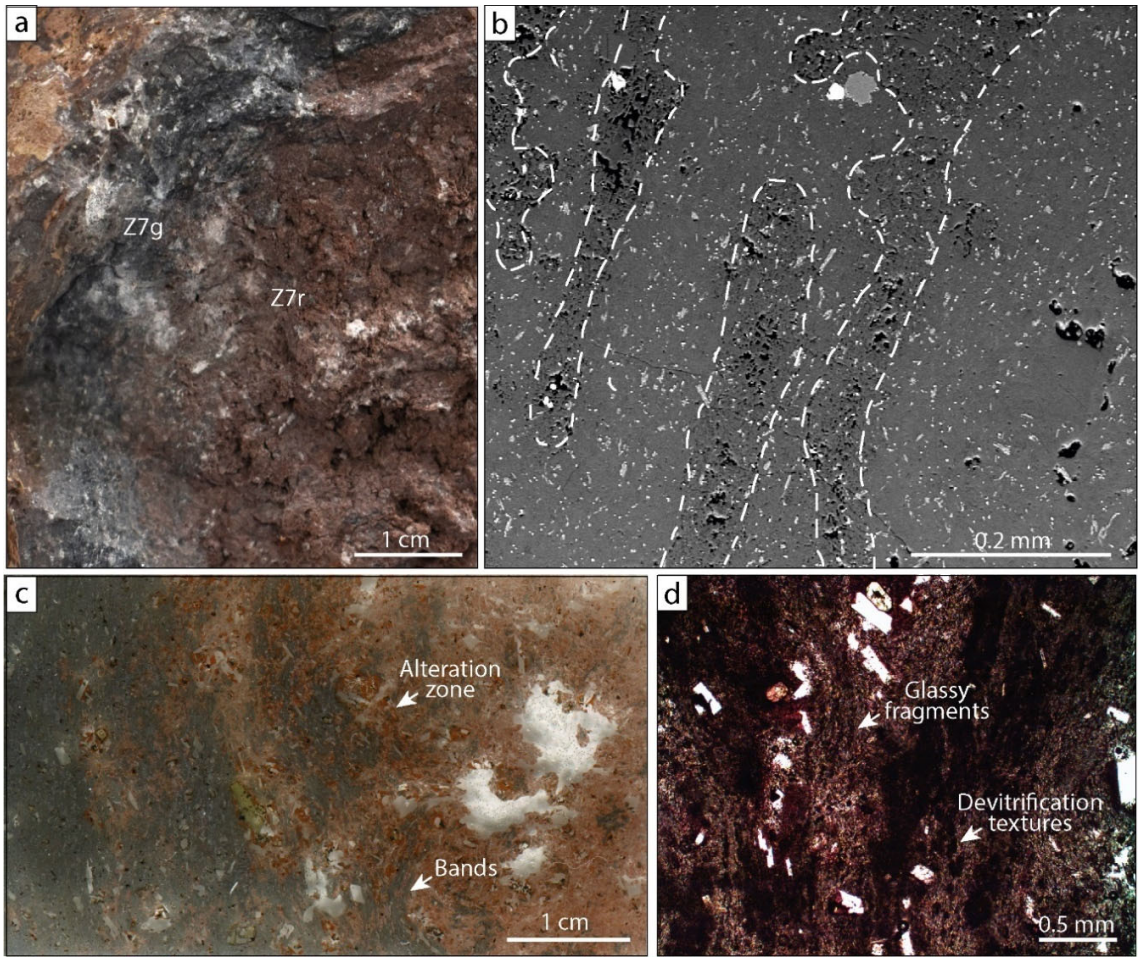

452

453 **Figure 8:** Textural aspects of Zone 7. **a** Hand specimen showing the contact between the grey
454 (Z7g) and the reddish (Z7r) domains. **b** SEM image at 400x magnification, showing the
455 intertwining of the two domains and their different porosities (in black). **c** Thin section scan
456 showing the interaction zone between the two domains, the reddish alteration and the grey
457 domain bands. **d** Thin section image in plane-polarised light, showing elongated glassy
458 fragments and devitrification textures.

4.2. Quantitative textural analysis

Here we describe the quantitative textural analysis of the zones described above, with data obtained using the following techniques: ImageJ, He pycnometer and FTIR. Figure 9 presents the sizes and shape of pores and their relative abundances in the samples analysed. Considering the pore major axis, the size of the pores in all samples measured ranged between 0.1-27 μm, with the most common sizes <12 μm (Fig. 9a). The pore size distribution of Z1 exhibits two distinct peaks, the first occurring under 18 μm with the largest area fraction of pores with sizes between 6 and 8 μm. The second peak is between 20-28 μm. The pores of the yellowish domain of Zone Z2 (Z2y) are dominated by pores with sizes between 2-6 μm, occupying around 2% of the total area fraction. Samples Z1 and Z2y have the largest pore sizes of all the samples measured. Z2g and Z7g are the zones with the smallest percentage of pores (total area fraction of 0.01 and 0.007 respectively) and with the smallest overall pore sizes. The pores in Z4 occupy a total area fraction of around 3%, the highest of the three grey domain samples analysed. The reddish (Z7r) domain pores in Z7 have two peaks as well as Z1. The first with pore sizes under 6 μm and the second between 6-12 μm.

As well as the pore sizes we also characterized the pore shapes by measuring their respective aspect ratios (a proxy for elongation). Most of the pores are moderately elongated, with aspect ratios of 0.4-0.6 (Fig. 9b). In all zones, pores with sizes <6 μm become more elongated as their size increases, varying from slightly elongated to moderately or even very elongated (Fig. 9a). In Z1 and Z2y, the pores between 6-14 μm also become less elongated as their size increases. For the pore size range of 20-22 μm, we found a percentage of extremely elongated pores only in samples Z1 and Z2y (Fig. 9a). In the eastern margin of the contact (Z7), the percentage of very elongated pores in the grey domain is less than half of that in the reddish domain (Fig. 9b). Conversely, the percentage of non-elongated pores in the grey domain is double that in the reddish domain. On the western margin of the contact (Z2), the percentage of very elongated pores in the grey domains is also only around half that in the yellow domains. Whereas the number of non-elongated pores is only around 15% different between the grey and yellow domains. During the measurement of pore geometries, we were also able to obtain information about their respective solidity factors (a proxy for roughness). For all zones, most of the pores have regular shapes and smooth margins, except for Z1, which has more concave-shaped pores. For Z2g and Z4, both parts of the grey domain, pores with solidity factors between 0.9 and 1 constitute 63% and 49% of the total pores, respectively.

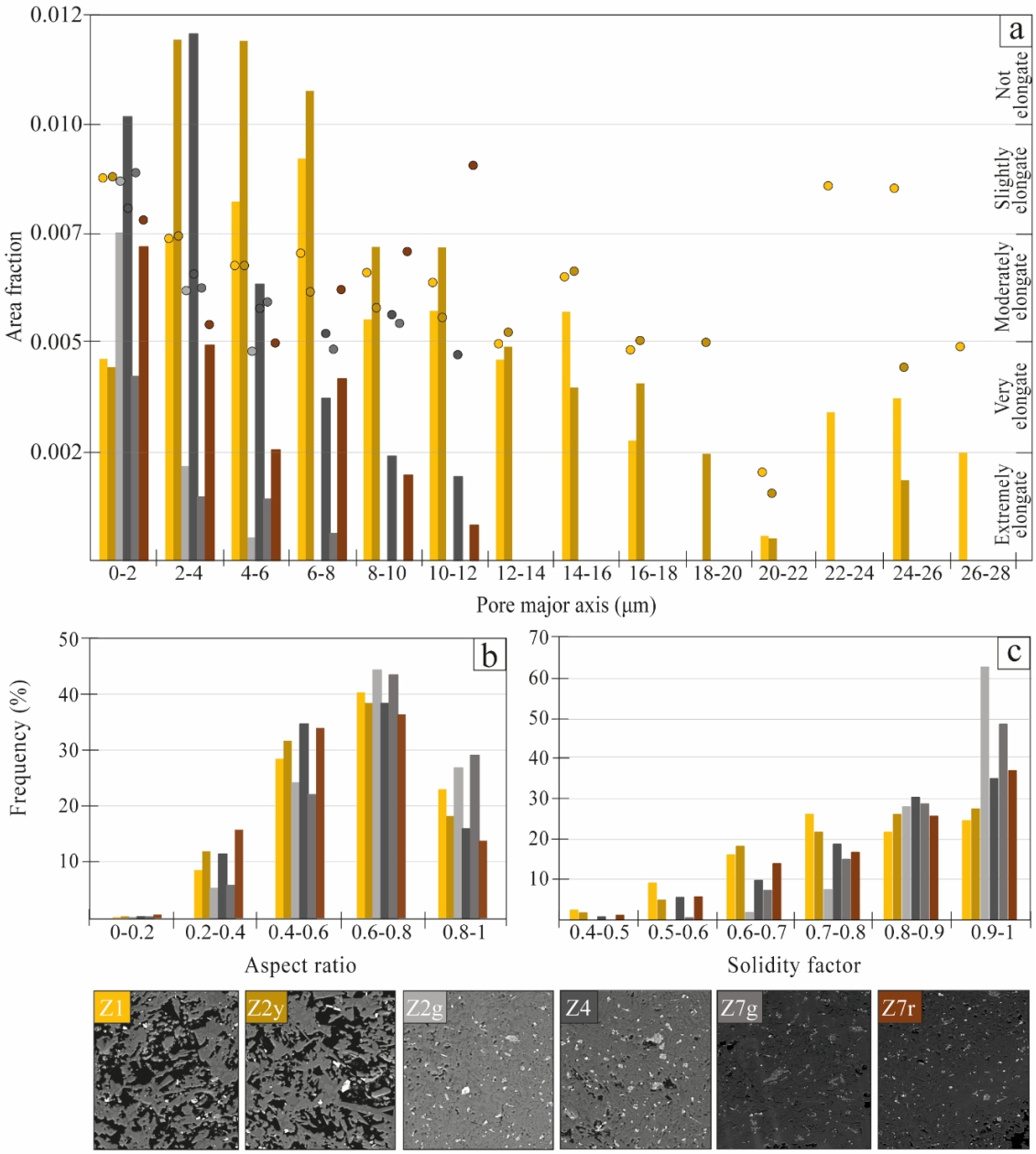

Figure 9: Quantitative textural analysis plots, legend at the bottom, with the SEM images associated with each zone analysed. **a)** Graph of area fraction versus pore major axis (bars). This demonstrates the fraction of area occupied by pores (y-axis-left) in a range of major axis lengths (x-axis), which are divided into 2 µm sections. Plus, the average aspect ratio versus the equivalent diameter (dots) in the same ranges of equivalent diameters (x-axis). The y-axis is divided into elongation categories. **b)** Graph of frequency versus aspect ratio. The y-axis is divided into frequency percentages with respect to total pores and the x-axis into elongation categories. c**)** Graph of frequency versus solidity factor. The y-axis is divided into frequency percentages with respect to total pores and the x-axis into solidity factor ranges.

The connected porosity, measured with the Helium pycnometer, differs between the three main domains. The directly measured porosity was 37% for the yellowish domain (measured on a Z1 sample), 15% for the reddish domain (measured on a Z7r sample), and 3% for the grey domain (Measured on a Z4 sample). The 2D total porosity measured from SEM images analysed with ImageJ exhibits a similar trend between the yellowish and grey domains, giving average porosities of 42% and 6% from Z1 and Z4 samples, respectively. However, an unusually lower average porosity value of 5% was obtained for the reddish domain. The same methodology was also used to measure the 2D porosity in the western and eastern contact zones. Both grey domain bands in Z2 and Z7 had an average porosity of 4%, whereas the yellow domain in Z2 had an average porosity of 39%. Measurements of the total water content of the glass focused on the western contact, i.e., Zones 1, 2 and 3. The results show overall low water contents which are lowest in the centre of the conduit and highest at the margins. In the yellow domain, the average H_2O_t content was 0.19±0.12%, whereas in the contact zone it was 0.13±0.07%, decreasing to 0.10±0.02% within the grey domain.

5. Discussion

5.1. Origins of the different conduit domains

The analysis of textures provides insights into the evolutionary history of the conduit and the magmatic processes that occurred during its formation. We interpret the outcrop as a fossilised volcanic conduit that has a fan-like shape suggesting that magma was approaching the surface (Geshi et al., 2020; Unwin et al., 2023), which is also supported by the low total water content (<1%) of all the conduit domains, indicating low confining pressure (Gonnermann and Manga, 2013). We consider the yellow domain as a product of primary fragmentation processes within the shallow conduit. This interpretation derives from the classification of this material as a polymictic lithic tuff with a relatively high porosity (37-42%). By contrast, the grey domain is interpreted as a product of magma effusion and densification (Wadsworth et al., 2020) classified primarily due to its relatively low porosity (3-6%) and its porphyritic and glomeroporphyritic texture. The intercalated and juxtaposed presence of these two domains, with such different textural characteristics, indicates that both behaviours occurred simultaneously. This implies that any eruption associated with the conduit would have likely formed a hybrid explosive-effusive style (Schipper et al., 2013; Wadsworth et al., 2022). However, this raises the key question of whether these two vastly different textures could be formed coevally? And, what is the nature of magma effusion during eruptions?

In the polymictic tuff (explosive), at least three different types of clasts were recognised. The different clast textures can be explained by multiple phases of magma fragmentation, vesiculation, and sintering over repeated events of decompression, generating diverse magma responses and products (Saubin et al., 2016; Jones et al., 2022). Regarding porosity, the pore

size distribution of Z1 and Z7r shows two peaks. This may be because the larger pores were formed through the coalescence of smaller vesicles, generating bimodal size distributions and irregular pore shapes (Adams et al., 2006; Shea et al., 2010). It could also suggest a later process of pore relaxation, where the rounding timescale is dependent on the pore size, being higher for largest pores, so the smaller pores will tend to be more spherical given the same stress and cooling history (Gardner et al., 2017). The origin of the population of larger pores could be associated with pre-eruptive bubble growth caused by prolonged ascent from deeper in the conduit (Saubin et al., 2016; Colombier et al., 2017).

The dense lava (effusive) is zoned, with the greatest difference in the number of fractures and phenocrysts or clusters. The zones in this domain generally exhibit similar textures, but Z4 is anomalous because the crystal populations generally do not exhibit preferential alignment, unlike the other three zones. This means that either the other zones were viscously flowing when the crystals formed, or the material was subsequently compressed, thus aligning the crystals. By contrast, Z4 was likely pooled, or cooled in a stationary manner without the presence of any dominating shear stress (Forien et al., 2011). The zones also exhibit different quantities of phenocrysts or clusters of phenocrysts, which may also have generated a zonation in viscosity and different responses to flow and fracturing. Bulk viscosity is lower when the concentration of crystals is lower (Llewellin and Manga, 2005; Sato, 2005). A lower viscosity also facilitates bubble nucleation and unhindered growth (Sparks, 1978; Bagdassarov et al., 1996; Cashman and Sparks, 2013), generating populations of vesicles with larger diameters. There are two dominant fracture orientations within Z3, which are approximately normal to one another. One set is predominantly perpendicular to the strike of the yellowish and grey bands, while the other set is parallel to the bands. The origin of the band-parallel fractures could relate to the difference in strength between the band material and the contacts between the bands (Cook and Gordon, 1964; Gudmundsson, 2011), while the origin of the band-perpendicular fractures may be related to horizontal compression accompanying densification. Z4 has the largest relative area occupied by pores (i.e., porosity) of the three grey domain samples analysed in the SEM, consistent with it containing the lowest proportion of phenocrysts. It also presents arcuate fractures which delimit tight fold structures. We interpret these features as deriving from the forcing of previously pooled and more viscous magma into arcuate forms within the central conduit.

Banding is a dominant textural characteristic of the outcrop, which provides clues as to magma emplacement and deformation mechanisms. The textural difference between the two predominant types of bands is that one set of bands has a relatively high porosity and the other is relatively dense, with a concomitantly lower porosity. However, both sets of bands are deformed, and this is manifested in the form of ductile folds at the centimetre to metre scale. Quantitative analysis of the shapes of pores that make up the porosity indicates that most pores are only moderately to slightly elongated in both sets of bands, despite distinctly different macro-textures (Fig. 9a). These apparently contradictory observations may reflect

588 the progressive effect of surface tension in relaxing bubble walls (pores) from initially
589 irregular shapes towards spherical shapes post-densification (Ellis et al., 2023). The dense
590 bands contain fragments of plagioclase phenocrysts which likely initially fragmented in the
591 conduit. This may indicate that the phenocrysts would have formed in the pyroclastic zone
592 but were later compacted and densified into dense bands. This interpretation is also supported
593 by observations of the sintering textures, where rounded globule-like glassy clasts are welded
594 onto crystal surfaces (Fig. 10a) (Wadsworth et al., 2020; Ryan et al., 2020) and where the
595 vesicles in the dense bands occur in low numbers and are specially rounded. This implies that
596 the observed pores have either a magma vesiculation origin or are formed when clasts sinter
597 and then relax making pore space (Wadsworth et al., 2016). However, the dense bands also
598 contain large numbers of euhedral plagioclase crystals (Fig. 10b), which could not have
599 formed by the same fragmental origin (Gavasci, 1989). This indicates that these crystals
600 either formed contemporaneously with the densification or may represent a previous stage of
601 crystallisation. This is supported by the observation that the euhedral plagioclase phenocrysts
602 are on average around fifty times larger than the sintered clasts (Fig. 10).
603

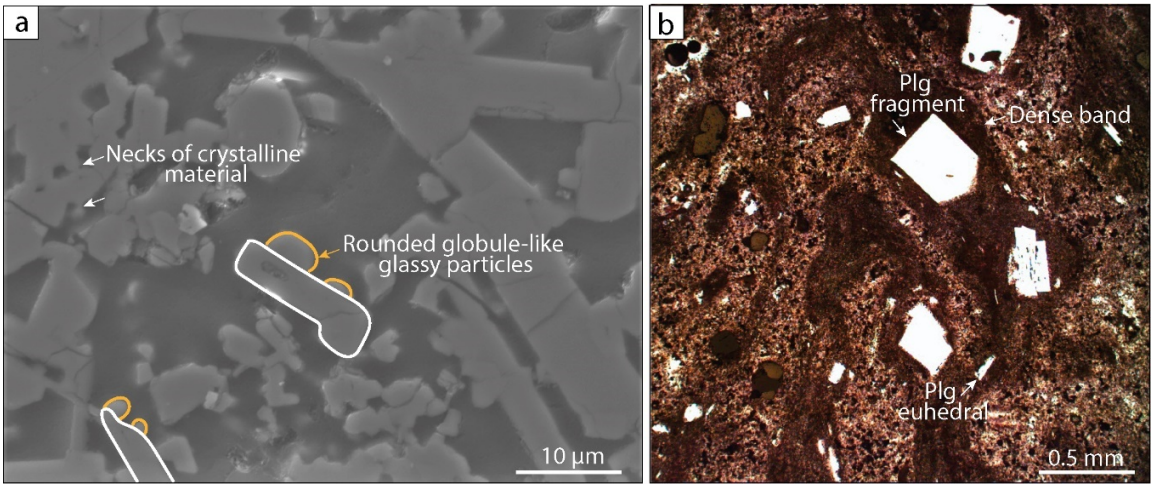

604
605 **Figure 10:** Evidence of fragmentation and densification processes. **a)** SEM image from Z2
606 exhibits sintering textures, with rounded globule-like glassy clasts, welded onto crystal
607 surfaces. White arrows show thin necks of crystalline material. **b)** Microscope image from
608 Z2 showing fragments and euhedral plagioclase crystals within a dense domain band.
609
610 The conditions and extent of fragmentation control the eruptive style (Jones et al., 2022), and
611 a transition from an explosive to an effusive style of behaviour probably occurs when factors
612 favouring fragmentation decrease or cease to exist (Castro and Gardner, 2008), tipping the
613 balance towards welding and recombination of fragmental material (Wadsworth et al., 2022;
614 Unwin et al., 2023). This change can be triggered by differences in magma decompression
615 rate (Alidibirov and Dingwell, 1996). Decompression events can trigger bubble nucleation
616 or brittle fragmentation, inducing different magmatic responses within the conduit. The
617 different magma responses generate different products that can vary in their texture,

depending on the decompression rate, magma porosity and volatile concentration (Saubin et al., 2016). One explanation for the juxtaposed different domains is that the porosity of the magma was heterogeneous on a small spatial scale, allowing banding to occur. Another possibility is that cyclic processes of fragmentation and compaction have occurred in the conduit (Kolzenburg and Russell, 2014; Trafton and Giachetti, 2022). We propose that the latter hypothesis is the most likely to produce the textures of the two interleaved domains with different levels of densification that we observe in this conduit.

5.2. Stages of conduit formation

We have integrated qualitative and quantitative textural data to propose a conceptual model of the evolving magmatic processes within the conduit (Fig. 11). The formation of the conduit and the observable textures can be divided into five principal phases. Phase one (I) begins with a predominantly explosive eruption generated by magma fragmentation, which fills the conduit with pyroclasts, gas and crystal fragments. During the waning phase, this fragmental material begins to deposit at the conduit walls (Unwin et al., 2023). The deposit contains lithics and mostly rounded intra-clast vesicles. Phase two (II) is defined by cyclic processes of both fragmentation and compaction, generating alternating bands of variably dense magma. Periods of sintering and densification, at the conduit margins, reduce the effective conduit width and in turn the rate of magma ascent and efficiency of fragmentation, inducing the input of denser, degassed magma pulses (Schipper et al., 2021). These pulses contain euhedral plagioclase crystals that are found exclusively within the dense bands. Densification processes then also permit the re-pressurisation of the conduit due to the lower magma permeability (Heap et al., 2019; Gaunt et al., 2020) which acts to increase the fragmentation rate in a cyclic manner (Kolzenburg and Russell, 2014). The dense magma also intrudes into the earlier pyroclastic material, generating the sinuous contacts that we observe in Z2. This dense magma could only have been derived from depth because it contains well-formed and non-fragmented plagioclase crystals.

Phase three (III) is characterized by a further waning of magma fragmentation rate – or a preponderance of more complete sintering – that leads to the upward emplacement of a largely coherent body of dense magma: apparently effusive eruption behaviour. The dense magma generates a plug that both seals the conduit and deforms the material deposited previously in phases one and two by internal compression (Wadsworth et al., 2020; Unwin et al., 2023). This internal force bends the bands and causes elongation of vesicles at the conduit margins. In phase three, the bands are characterized by the presence of both euhedral and fragmented plagioclase. In addition, part of the early fragmental material could also have been trapped in the centre of the conduit, generating pockets of relatively high porosity lithic tuff with devitrified rims, as seen in Figure 7c. This observation supports the idea that the dense plug formed in a later phase, after the main fragmentation event, as the pyroclastic material must have existed to become entrained within the plug. Phase four (IV) is

represented by the compaction and further deformation of the intercalated bands, generating glassy fiamme and folded textures. Phases three and four are essentially synchronous since the process of compaction requires compression from the dense magma plug material. In the final phase, phase five (V), when the eruption and magma input have essentially ceased, pores (whether "true" magmatic vesicles or inter-clast pores following sintering) relax towards spherical shapes within the still-hot magma at the conduit margins (Ellis et al., 2023). In this phase, as the dense magma cools, it fractures preferentially along the plane of the flow direction, generating quasi-fold-like textures within the magma plug, as observed within the rhyolitic lava at Cordón Caulle (Magnall et al., 2018).

Based on the narrow conduit size at this location, we assume that the associated magma discharge at this point on the eruptive fissure was relatively short-lived, perhaps lasting only hours to days. Indeed, the narrowness and relative textural simplicity at the tip of a dissected silicic dyke at Krafla, Iceland (Tuffen and Castro, 2009) contrasts with the greater textural complexity and width near the fissure centre, indicative of more prolonged magma output following focussing of magma emission on the fissure. There is little evidence of an extensive fissure at the Nevados de Chillan site but the possibility that the exposed conduit represents a lateral, thinner, termination of a larger fissure cannot be ruled out. Focussing of fissure-fed silicic eruptions in Chile has also been inferred for a 1960-61 eruption of Cordón Caulle (Lara et al., 2004). The explosive phase of the eruption would likely have been the shortest phase, quickly leading to hybrid explosive-effusive behaviour and then becoming dominated by effusive lava emission. We also noted that, texturally, the conduit is asymmetric, where evidence of banded hybrid activity is restricted to a zone on the eastern margin of the conduit that is much narrower than that on the western margin.

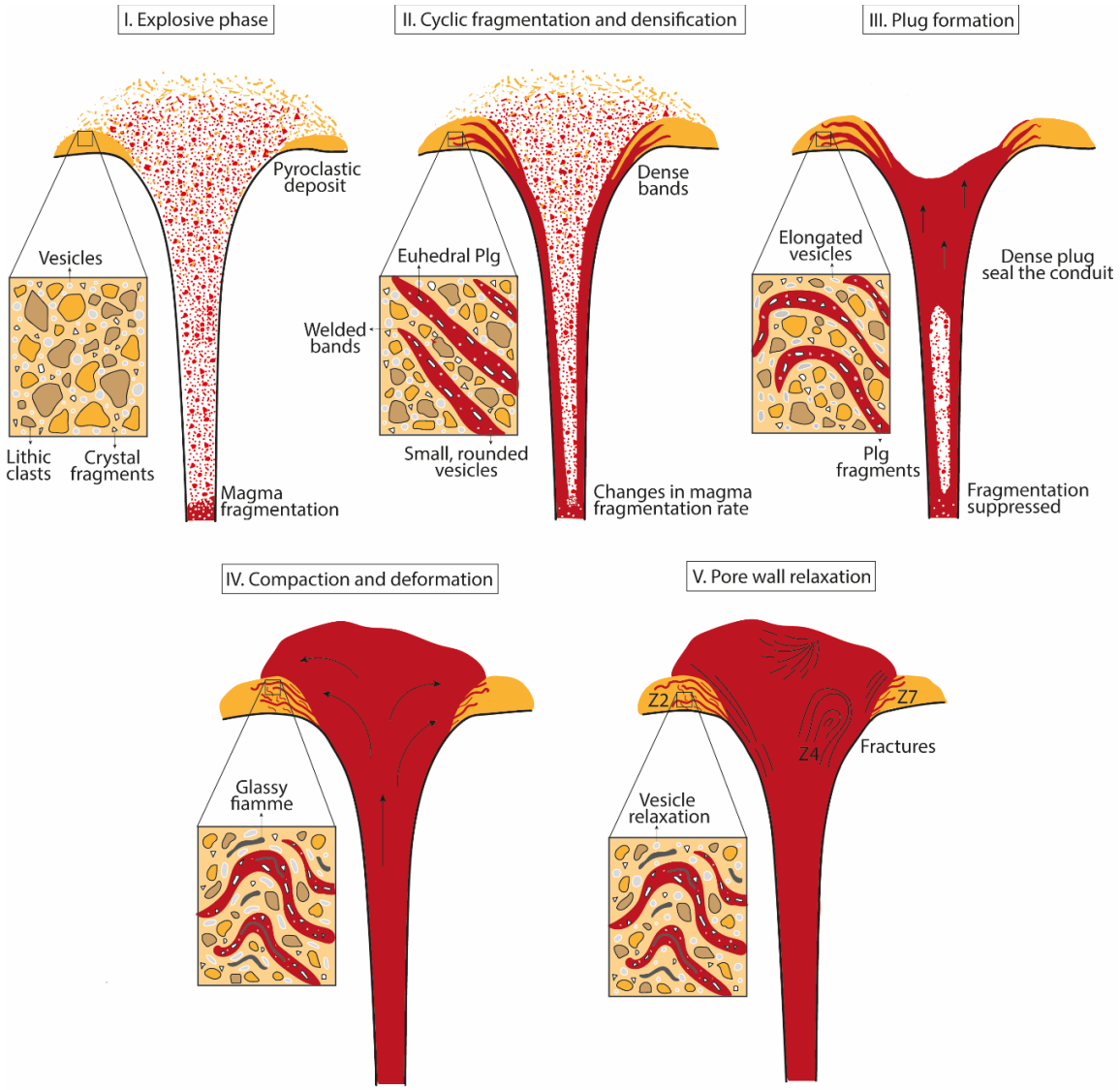

Figure 11: Summary of evolving processes within five predominant phases, derived from textural observations of our studied shallow conduit. The inserts in the images described the evolution of textures predominantly within the banded section that makes up the zone we classify as Z2.

5.3. Comparison with other conduits of different sizes

Dissected conduits or vents provide relevant information about the magmatic processes that occurred during their formation. Here we present a comparison with three other conduits of different sizes: Mule Creek vent (USA), Thumall conduit (Iceland) and Cordón Caulle (Chile). Mule Creek is a dissected silicic vent with a width of several tens of metres (Fig. 12a) and is located in New Mexico, USA (Unwin et al., 2023). Although the most remarkable feature of this vent is the formation of tuffisites (fractures filled with pyroclastic material;

699 Fig. 12b), some processes related to particle densification are similar to those observed in our
700 NCVC flank conduit. For example, Unwin et al., (2023) described the formation of a 1-7 m
701 wide dense glassy unit at the margin of the conduit, formed from the accretion and welding
702 of ash particles. This unit shares many similarities with our grey domain bands in Z2, albeit
703 at a much larger scale. Since the Mule Creek conduit was wider, it would likely have cooled
704 more slowly, allowing a longer period of sintering than would have been experienced at our
705 Nevados de Chillan flank conduit (Kolzenburg et al., 2019).
706
707 The flow-deformed tuffisites described at Mule Creek are also texturally similar to those
708 trapped bands described in Z6, which generated the star-shaped high porosity lithic tuff with
709 devitrified margins. The origin of this clastic fill feature is from an erupting and bypassing
710 dispersion travelling up a volcanic conduit before conduit sealing. This would explain the
711 presence of part of the yellow domain in such a central and uppermost part of the exposed
712 height of the conduit. Wadsworth et al. (2014) and Heap et al. (2019) show that sintering and
713 welding processes can also be observed within tuffisites, which are essentially identical to
714 the initial stage of a pyroclast-filled conduit, but on a much smaller scale, demonstrating that
715 it is a cross-scale process (Schipper et al., 2021; Unwin et al., 2023). The Thumall conduit
716 (Torfajökull, Iceland) is intermediate in scale between the NCVC flank conduit and the Mule
717 Creek vent, with a width of approximately 10 metres and an exposed height of 15 m (Fig.
718 12c; Tuffen and Dingwell, 2005). In this outcrop, a dense glassy unit was also identified in
719 the outermost parts of the conduit, approximately 5 metres wide. The proposed genesis of
720 this zone relates sintering with cohesive ductile deformation, which generates banding and
721 folding within the cataclastic zone (Fig. 12d), similar to the textures observed in the contact
722 zones of the NCVC flank conduit. However, the bands are interpreted as being formed by
723 gas transport of particles through the fracture system in a cataclasis-type process, and the
724 observed differences in colour are due to varying concentrations of metallic oxide microlites
725 (Tuffen and Dingwell, 2005).
726

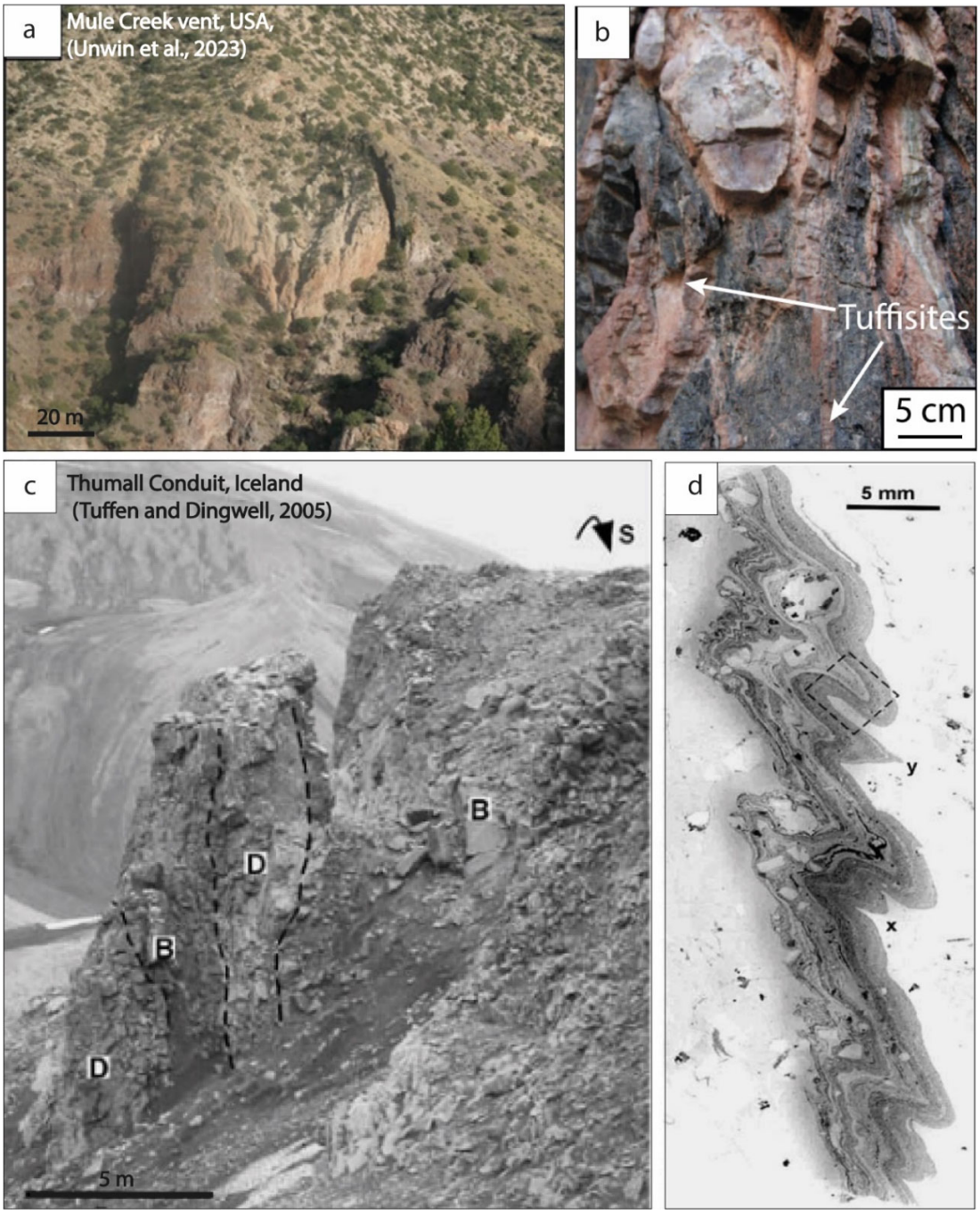

Figure 12: Photos at different scales of the Mule Creek vent (a, b) from Unwin et al. (2023); and the Thumall conduit (c, d) from Tuffen and Dingwell (2005).

Finally, while it is not possible to directly observe subsurface structures in the conduit of Cordon Caulle, several interpretations related to explosive-effusive eruptive style transitions have been made from observations of the eruption and its products (Castro et al., 2014; Schipper et al., 2013; 2021; Wadsworth et al., 2020; 2022; Farquharson et al., 2022). Schipper et al. (2021) focus their work on ejecta as they represent the best available evidence of the

736 textural state of magma in the shallow conduit. There is evidence that, in addition to being
737 on a much larger scale, the transition in eruptive style occurred over several months during
738 the last eruptive period of Cordon Caulle. This duration likely greatly exceeds that of the
739 activity inferred on the NCVC flank conduit. The bombs studied from Cordon Caulle are
740 evidence that, even at this larger scale, vastly different textural states can be generated and
741 closely juxtaposed. However, Schipper et al. (2021) and Wadsworth et al. (2022) propose that
742 the transition in eruptive style did not involve a decrease in the rate of fragmentation, only
743 that sintering on the walls of the conduit slowly reduced the conduit width and eventually
744 sealed it. By contrast, the intercalated textural domains in the conduit studied in this work
745 require a cyclic process of fragmentation and compaction that necessarily involves
746 potentially several changes in the degree of fragmentation at this shallow level over time
747 (Trafton and Giachetti, 2022). The evolution of fragmentation is then not necessarily a
748 singular process accompanied by the self-extinction of the eruption, as is the case of Cordón
749 Caulle (Wadsworth et al., 2020), but may instead involve several periods of increased or
750 decreased fragmentation and compaction rates. We suggest that the transition could have
751 been associated with the onset of arrival of coherent melt at the shallowest levels in the vent,
752 which could explain the survival of euhedral plagioclase in the Z2 and Z7 bands. A vexed
753 question is whether this late-arriving melt was truly coherent, or simply less intensely
754 fragmented, thus permitting a greater proportion of magmatic phenocrysts to evade fracture.
755 The exposed conduit studied on the SW flank of Nevados de Chillan is at least an order of
756 magnitude thinner, at around 1 m wide, than the other three examples discussed here.
757 However, dykes of similar thickness (between 1 to 10 m wide) have been shown to commonly
758 feed flank eruptions (Geshi and Neri., 2014; Browning et al., 2015, Ruz, et al., 2020, Geshi
759 et al., 2020). As such, the similarity of textural observations observed across the scales
760 mentioned indicate universality of shallow conduit processes.
761
762 ## 6. Conclusions
763
764 1. We document a shallow, narrow silicic conduit that crops out on the flanks of Nevados
765 de Chillán Volcanic Complex, Chile. Field, textural, and microstructural observations
766 from such outcrops and its internal domains provide evidence of conduit evolution
767 processes that can be linked to and compared with other conduits and eruptions of
768 different sizes.
769 2. The different porosities of the domains reflect different degrees of densification, where
770 the lowest porosity (4%) is found in the dense bands of both contact zones. The shape
771 distribution of pores in each domain does not show any significant change, which may
772 evidence late relaxation processes post-sintering, returning them to their regular, mainly
773 rounded forms. The presence of euhedral plagioclase phenocrysts, which are
774 significantly larger than the sintered clasts, demonstrates that the dense bands cannot
775 originate solely from compaction and welding of the fine-fragmented pyroclastic

776 domain, but that a magma pulse has arrived in the upper conduit that has largely evaded
777 fracturing and damage to its pre-existing phenocryst population.
778 3. Five principal phases of the evolution of the conduit were identified, according to the
779 qualitative and quantitative analysis of the conduit domains and their textures; (I) an
780 explosive phase where the conduit is filled with pyroclastic material, (II) a cyclic process
781 of fragmentation and densification within the conduit that generates intercalation of the
782 porous and dense domains and leads to a hybrid explosive-effusive phase, (III) the
783 formation of a dense magma plug that eventually seals the conduit and deforms the
784 already formed vesicles, pores, and bands, (IV) compaction of the pyroclastic domain
785 due to the ascent of the plug generating micro-folds and, glassy fiamme, representing
786 predominantly coherent, effusive magma ascent, and (V) a final phase of pore relaxation
787 and fracturing of the late-emplaced dense magma.
788 4. The conceptual model generated provides an enhanced understanding of eruption style
789 transition and conduit processes, which can be applied to other conduits with similar
790 characteristics and can be incorporated into existing models. These ideas could be further
791 developed with an analysis of the temporal evolution of textures, porosity, and
792 permeability to give a more accurate timescale for each phase of the process.
793
794 **Data availability statement**
795
796 All data and materials are available by request to the author.
797
798 **CRediT authorship contribution**
799
800 **Flavia Rojas:** Conceptualization, Methodology, Formal analysis, Investigation, Writing –
801 Original draft, Visualization. **John Browning:** Conceptualization, Methodology, Formal
802 analysis, Investigation, Writing – Review & Editing. **Hugh Tuffen**: Conceptualization,
803 Methodology, Investigation, Resources, Writing – Review & Editing. **José Cembrano:**
804 Conceptualization, Writing – Review & Editing, Funding acquisition. **Javier Espinosa-**
805 **Leal:** Conceptualization, Investigation. **Holly E. Unwin:** Conceptualization, Investigation,
806 Writing – Review & Editing. **Thomas M. Mitchell:** Investigation, Writing – Review &
807 Editing. **Karin Hofer-Apostolidis:** Investigation**. Philip G. Meredith:** Investigation,
808 Writing – Review & Editing.
809
810 **Declaration of competing interest**
811
812 The authors declare that they have no known competing financial interests or personal
813 relationships that could have appeared to influence the work reported in this paper.
814
815 **Acknowledgements**
816

This work was funded by the Chilean National Fund for Scientific and Technological Development (FONDECYT n°1210591). FR and JB acknowledge a UC-UCL open seed fund 797 award. HEU publishes with permission from the Executive Director of the British Geological Survey.

References

Adams, N., Hughton, B. and Hildreth, W. (2006). Abrupt transitions during sustained explosive eruptions: examples from the 1912 eruption of Novarupta, Alaska. *Bulletin of Volcanology, 69, 189-206.* https://doi.org/10.1007/s00445-006-0067-4

Alfano, F., Bonadonna, C. and Gurioli, L. (2012). Insights into eruption dynamics from textural analysis: the case of the May 2008, Chaitén eruption. *Bulletin of Volcanology, 74, 2095–2108.* https://doi.org/10.1007/s00445-012-0648-3

Alidibirov, M. and Dingwell, D. (1996). Magma fragmentation by rapid decompression. *Nature, 380, 146-148*. https://doi.org/10.1038/380146a0

Benet, D., Costa, F., Pedreros, G. and Cardona, C. (2021). The volcanic ash record of shallow magma intrusion and dome emplacement at Nevados de Chillán Volcanic complex, Chile. *Journal of Volcanology and Geothermal Research, 471, 107308.* https://doi.org/10.1016/j.jvolgeores.2021.107308

Bagdassarov, N.S., Dingwell, D.B. and Wilding, M.C., 1996. Rhyolite magma degassing: an experimental study of melt vesiculation. *Bulletin of volcanology, 57, 587-601*. https://doi.org/10.1007/s004450050114

Bistacchi, A., Mittempergher, S., & Martinelli, M. (2022). Digital outcrop model reconstruction and interpretation. *3D Digital Geological Models: From Terrestrial Outcrops to Planetary Surfaces, 11-32*. https://doi.org/10.1002/9781119313922.ch2

Brett, C., Clarke, A. and de Michieli, M. (2020). Volcanic conduit controls on effusive-explosive transitions and the 2010 eruption of Merapi Volcano (Indonesia). *Journal of Volcanology and Geothermal Research, 392, 106767.* https://doi.org/10.1016/j.jvolgeores.2019.106767

Browning, J., Drymoni, K. and Gudmundsson, A., 2015. Forecasting magma-chamber rupture at Santorini volcano, Greece. *Scientific reports*, *5*(1), p.15785. https://doi.org/10.1038/srep15785

Burgisser, A. and Gardner, J. (2004). Experimental constraints on degassing and permeability in volcanic conduit flow. *Bulletin of Volcanology, 67, 42-56*. https://doi.org/10.1007/s00445-004-0359-5

Cardona, C., Gil-Cruz, F., Franco-Marín, L., San Martín, J., Valderrama, O., Lazo, J., Cartes, C., Morales, S., Hernández, E., Quijada, J., Pinto, C., Vidal, M., Bravo, C., Pedreros, G., Contreras, M., Figueroa, M., Córdova, L., Mardones, C., Alarcón, A., Velásquez, G. and Bucarey, C. (2021). Volcanic activity accompanying the emplacement of dacitic lava domes and effusion of lava flows at Nevados de Chillán Volcanic Complex – Chilean Andes (2012 to 2020). *Journal of Volcanology and Geothermal*

Research, 420, 107409, 0377-0273. https://doi.org/10.1016/j.jvolgeores.2021.107409

Cashman, K. and Sparks, S. (2013). How volcanoes work: A 25-year perspective. *Geological Society of America Bulletin, 125, 5, 664-690.* https://doi.org/10.1130/B30720.1

Cashman, K. V., Mangan, M. T., & Newman, S. (1994). Surface degassing and modifications to vesicle size distributions in active basalt flows. *Journal of volcanology and geothermal research, 61(1-2), 45-68*. https://doi.org/10.1016/0377-0273(94)00015-8

Cassidy, M., Magna, M., Cashman, K. and Bachmann, O. (2018). Controls on explosive-effusive volcanic eruption styles. *Nature Communications, 9, 2839.* https://doi.org/10.1038/s41467-018-05293-3

Castro, J., Bindeman, I., Tuffen, H. and Schipper, I. (2014). Explosive origin of silicic lava: Textural and δD–H2O evidence for pyroclastic degassing during rhyolite effusion. *Earth and Planetary Science Letters, 405, 52-61.* https://doi.org/10.1016/j.epsl.2014.08.012

Castro, J. and Gardner, J. (2008). Did magma ascent rate control the explosive-effusive transition at the Inyo volcanic chain, California? *Geology, 36(4), 279-282.* https://doi.org/10.1130/G24453A.1

Cembrano, J. and Lara, L. (2009). The link between Volcanism and tectonics in the southern volcanic zone of the Chilean Andes: A review. *Tectonophysics, 471, 1-2, 96-113.* https://doi.org/10.1016/j.tecto.2009.02.038

Chen, Y., Zou, C., Mastalerz, M., Hu, S., Gasaway, C. and Tao, X. (2015). Applications of Micro-Fourier Transform Infrared Spectroscopy (FTIR) in the Geological Sciences - A Review. *International Journal of Molecular Sciences, 16, 30223-30250.* https://doi.org/10.3390/ijms161226227

Colombier, M., Wadsworth, F., Gurioli, L., Scheu, B., Kueppers, U., Di Muro, A. and Dingwell, D. (2017). The evolution of pore connectivity in volcanic rocks. *Earth and Planetary Science Letters, 462, 99-109.* https://doi.org/10.1016/j.epsl.2017.01.011

Columbu, S., Mulas, M., Mundula, F. and Cioni, R. (2021). Strategies for helium pycnometer density measurements of welded ignimbrite rocks. *Measurement, 173, 108640.* https://doi.org/10.1016/j.measurement.2020.108640

Cook, J. and Gordon, J.E. (1964). A mechanism for the control of crack propagation in all-brittle systems. Proceedings of the Royal Society of London. Series A. *Mathematical and Physical Sciences, 282(1391), 508-520.* https://doi.org/10.1098/rspa.1964.0248

Diniega, S., Smrekar, E., Anderson, S. and Stofan, E. R. (2013). The influence of temperature-dependent viscosity on lava flow dynamics. *Journal of Geophysical Research: Earth Surface, 118, 1516-1532.* https://doi.org/10.1002/jgrf.20111

Dixon, H., Murphy, M., Sparks, S., Chávez, R., Naranjo, J., Dunkley, P., Young, S., Gilbert, J. and Princle, M. (1999). The geology of Nevados de Chillán volcano, Chile. *Revista Geológica de Chile, 26, 2, 0716-0208.* http://dx.doi.org/10.4067/S0716-02081999000200006

898 Eichelberger, J., Carrigan, C., Westrich, H. and Price, R.H. (1986). Non-explosive silicic
899 volcanism. *Nature, 323, 598-602.* https://doi.org/10.1038/323598a0
900 Ellis, B. S., Pimentel, A., Cortes-Calderon, E. A., Moser, Z., Baumann, N., Bachmann, O., &
901 Wadsworth, F. B. (2023). Obsidian clasts as sintered remnants of agglutination
902 processes in volcanic conduits, evidence from the Pepom tephras (Sete Cidades), São
903 Miguel, Azores. *Chemical Geology, 638, 121694.*
904 https://doi.org/10.1016/j.chemgeo.2023.121694
905 Farquharson, J. I., Tuffen, H., Wadsworth, F. B., Castro, J. M., Unwin, H., & Schipper, C. I.
906 (2022). In-conduit capture of sub-micron volcanic ash particles via turbophoresis and
907 sintering. *Nature Communications, 13(1), 4713*. https://doi.org/10.1038/s41467-022-
908 32522-7
909 Forien, M., Arbaret, L., Burgisser, A., & Champallier, R. (2011). Experimental constrains on
910 shear-induced crystal breakage in magmas. *Journal of Geophysical Research: Solid*
911 *Earth, 116(B8).* https://doi.org/10.1029/2010JB008026
912 Gaunt, H.E., Burgisser, A., Mothes, P.A., Browning, J., Meredith, P.G., Criollo, E. and
913 Bernard, B. (2020). Triggering of the powerful 14 july 2013 vulcanian explosion at
914 Tungurahua volcano, Ecuador. *Journal of Volcanology and Geothermal Research,*
915 *392, p.106762.* https://doi.org/10.1016/j.jvolgeores.2019.106762
916 Gardner, J. E., Llewellin, E. W., Watkins, J. M., & Befus, K. S. (2017). Formation of obsidian
917 pyroclasts by sintering of ash particles in the volcanic conduit. *Earth and Planetary*
918 *Science Letters, 459, 252-263*. https://doi.org/10.1016/j.epsl.2016.11.037
919 Gavasci, A.T. (1989). *Textures of igneous rocks. In: Petrology*. Encyclopedia of Earth
920 Science. Springer, Boston, MA.
921 Geshi, N. and Neri, M., 2014. Dynamic feeder dyke systems in basaltic volcanoes: the
922 exceptional example of the 1809 Etna eruption (Italy). *Frontiers in Earth Science*, *2*,
923 p.13. https://doi.org/10.3389/feart.2014.00013
924 Geshi, N., Browning, J. and Kusumoto, S. (2020). Magmatic overpressures, volatile
925 exsolution and potential explosivity of fissure eruptions inferred via dike aspect
926 ratios. *Scientific reports, 10(1), p.9406.* https://doi.org/10.1186/s40623-022-01577-7
927 Gonnermann, H. M., & Manga, M. (2013). Dynamics of magma ascent in the. *Modeling*
928 *volcanic processes: The physics and mathematics of volcanism,* 55.
929 Gonnermann, H. and Manga, M. (2007). The fluid mechanics inside a volcano. *Annual*
930 *Review of Fluid Mechanics, 39, 321-356.*
931 https://doi.org/10.1146/annurev.fluid.39.050905.110207
932 Gudmundsson, A. (2011). Rock fractures in geological processes. Cambridge University
933 Press.
934 Heap, M. J., Troll, V. R., Kushnir, A. R., Gilg, H. A., Collinson, A. S., Deegan, F. M.,
935 Darmawan, H., Sereohine, N., Neuberg, J. and Walter, T. R. (2019). Hydrothermal
936 alteration of andesitic lava domes can lead to explosive volcanic behaviour. *Nature*
937 *communications*, *10*(1), 5063. https://doi.org/10.1038/s41467-019-13102-8

938 Heiken, G., Wohletz, K., & Eichelberger, J. (1988). Fracture fillings and intrusive pyroclasts,
939 Inyo Domes, California. *Journal of Geophysical Research: Solid Earth, 93(B5),*
940 *4335-4350*. https://doi.org/10.1029/JB093iB05p04335
941 Hu, Z., Zhang, R., Zhu, K., Li, D., Jin, Y., Guo, W., Liu, X., Zhang, X. and Zhang, Q. (2023).
942 Probing the Pore Structure of the Berea Sandstone by Using X-ray Micro-CT in
943 Combination with ImageJ Software. *Minerals, 13(3), 360.*
944 https://doi.org/10.3390/min13030360
945 James, M. R., Robson, S., d'Oleire-Oltmanns, S., & Niethammer, U. (2017). Optimising UAV
946 topographic surveys processed with structure-from-motion: Ground control quality,
947 quantity and bundle adjustment. *Geomorphology, 280, 51-66.*
948 https://doi.org/10.1016/j.geomorph.2016.11.021
949 Jaupart, C. and Allègre, C. (1991). Gas content, eruption rate and instabilities of eruption
950 regime in silicic volcanoes. *Earth and Planetary Science Letters, 102, 413-429.*
951 https://doi.org/10.1016/0012-821X(91)90032-D
952 Jones, T., Cashman, K., Liu, E., Rust, A. and Scheu, B. (2022). Magma fragmentation: a
953 perspective on emerging topics and future directions. *Bulletin of Volcanology, 84:45.*
954 https://doi.org/10.1007/s00445-022-01555-7
955 Kendrick, J.E., Lavallée, Y., Hess, K-U., Heap, M., Gaunt, H.E., Meredith, P.G. and
956 Dingwell, D. (2013). Tracking the permeable porous network during strain-dependent
957 magmatic flow. *Journal of Volcanology and Geothermal Research, 260, 117-126.*
958 https://doi.org/10.1016/j.jvolgeores.2013.05.012
959 Kolzenburg, S., Ryan, A. G., & Russell, J. K. (2019). Permeability evolution during non-
960 isothermal compaction in volcanic conduits and tuffisite veins: Implications for
961 pressure monitoring of volcanic edifices. *Earth and Planetary Science Letters, 527,*
962 *115783*. https://doi.org/10.1016/j.epsl.2019.115783
963 Kolzenburg, S., & Russell, J. K. (2014). Welding of pyroclastic conduit infill: A mechanism
964 for cyclical explosive eruptions. *Journal of Geophysical Research: Solid Earth,*
965 *119(7), 5305-5323*. https://doi.org/10.1002/2013JB010931
966 Kumar, A., Garia, S., Ravi, K. and Nair, A.M. (2018). Porosity estimation by digital image
967 analysis. *ONGC Bulletin, 53(2), 59-72.*
968 Lara, L. E., Naranjo, J. A., & Moreno, H. (2004). Rhyodacitic fissure eruption in Southern
969 Andes (Cordón Caulle; 40.5 S) after the 1960 (Mw: 9.5) Chilean earthquake: a
970 structural interpretation. *Journal of Volcanology and Geothermal Research, 138(1-2),*
971 *127-138*. https://doi.org/10.1016/j.jvolgeores.2004.06.009
972 Llewellin, E. and Manga, M. (2005). Bubble suspension rheology and implications for
973 conduit flow. *Journal of Volcanology and Geothermal Research, 143, 205-217.*
974 https://doi.org/10.1016/j.jvolgeores.2004.09.018
975 Lupi, M., Trippanera, D., Gonzalez, D., D'amico, S., Acocella, V., Cabello, C., Meulle-Stef,
976 M. and Tassara, A. (2020). Transient tectonic regimes imposed by megathrust
977 earthquakes and the growth of NW-trending volcanic systems in the Southern Andes.
978 *Tectonophysics, 774, 228204*. https://doi.org/10.1016/j.tecto.2019.228204

Magnall, N. A. (2018). *Commonalities in the emplacement of cooling-limited lavas: insights from the 2011-2012 Cordón Caulle rhyolitic eruption.* Lancaster University (United Kingdom).

Melnik, O., Barmin, A. and Sparks, S. (2005). Dynamics of magma flow inside volcanic conduits with bubble overpressure buildup and gas loss through permeable magma. *Journal of Volcanology and Geothermal Research, 143, 53-68.* https://doi.org/10.1016/j.jvolgeores.2004.09.010

Moussallam, Y., Bani, P., Schipper, I., Cardona, C., Franco, F., Barnie, T., Amigo, A., Curtis, A., Peters, N., Aiuppa, A., Giudice, G. and Oppenheimer, C. (2018). Unrest at the Nevados de Chillán volcanic complex: a failed or yet to unfold magmatic eruption? *Volcanica, 1(1), 19-32.* https://hal.science/hal-03881749

Naranjo, J., Gilbert, J. and Sparks, S. *Geología del complejo volcánico Nevados de Chillán, Región del Biobío.* Servicio Nacional de Geología y Minería, Carta Geológica de Chile, Serie Geología Básica, 114 (2008), p. 28.

Nguyen, C., Gonnermann, H. and Houghton, B. (2014). Explosive to effusive transition during the largest volcanic eruption of the 20th century (Novarupta 1912, Alaska). *Geology, 42(8), 703–706.* https://doi.org/10.1130/G35593.1

Nishikida, K., Nishio, E. and Hannah, R. (1996). Selected Applications of Modern FT-IR Techniques. CRC Press.

Novoa, C., Gerbault, M., Remy, D., Cembrano, J., Lara, L.E., Ruz-Ginouves, J., Tassara, A., Baez, J.C., Hassani, R., Bonvalot, S. and Contreras-Arratia, G. (2022). The 2011 Cordón Caulle eruption triggered by slip on the Liquiñe-Ofqui fault system. *Earth and Planetary Science Letters, 583, 117386.* https://doi.org/10.1016/j.epsl.2022.117386

Oyarzún, A., Lara, L. and Tassara, A. (2022). Decoding the plumbing system of Nevados de Chillán Volcanic complex, Southern Andes. *Journal of Volcanology and Geothermal Research, 422, 0377-0273.* https://doi.org/10.1016/j.jvolgeores.2021.107455

Papale, P. (1999). Strain-induced magma fragmentation in explosive eruptions. *Nature, 397, 425-428.* https://doi.org/10.1038/17109

Preece, K., Gertisser, R., Barclay, J., Charbonnier, S., Komorowski, JC. and Herd, R. (2016). Transitions between explosive and effusive phases during the cataclysmic 2010 eruption of Merapi volcano, Java, Indonesia. *Bulletin of Volcanology, 78(54).* https://doi.org/10.1007/s00445-016-1046-z

Ryan, A., Russel, J., Heap, M., Zimmerman, M. and Wadsworth, F. (2020). Timescales of porosity and permeability loss by solid-state sintering. *Earth and Planetary Science Letters, 549, 116533.* https://doi.org/10.1016/j.epsl.2020.116533

Ruz, J., Browning, J., Cembrano, J., Iturrieta, P., Gerbault, M. and Sielfeld, G., 2020. Field observations and numerical models of a Pleistocene-Holocene feeder dyke swarm associated with a fissure complex to the east of the Tatara-San Pedro-Pellado complex, Southern Volcanic Zone, Chile. *Journal of Volcanology and Geothermal Research*, *404*, p.107033. https://doi.org/10.1016/j.jvolgeores.2020.107033

Sato, H., 2005. Viscosity measurement of subliquidus magmas: 1707 basalt of Fuji volcano. *Journal of Mineralogical and Petrological Sciences, 100(4), pp.133-142.* https://doi.org/10.2465/jmps.100.133

Saubin, E., Tuffen, H., Gurioli, L., Owen, J., Castro, J.M., Berlo, K., McGowan, E., Schipper, I. and Wehbe, K. (2016). Conduit dynamics in transitional rhyolitic activity recorded by tuffisite vein textures from the 2008-2009 Chaitén eruption. *Frontiers in Earth Science, 4(59).* https://doi.org/10.3389/feart.2016.00059

Schipper, I., Castro, J., Kennedy, B., Tuffen, H., Whattam, J., Wadsworth, F., Paisley, R., Fitzgerald, R., Rhodes, E., Schaefer, L., Ashwell, P., Forte, P., Seropian, G. and Alloway, B. (2021). Silicic conduits as supersized tuffisites: Clastogenic influences on shifting eruption styles at Cordón Caulle volcano (Chile). *Bulletin of Volcanology, 83(11).* https://doi.org/10.1007/s00445-020-01432-1

Schipper, I., Castro, J., Tuffen, H., James, M. and How, P. (2013). Shallow vent architecture during hybrid explosive–effusive activity at Cordón Caulle (Chile, 2011–12): Evidence from direct observations and pyroclast textures. *Journal of Volcanology and Geothermal Research, 262, 25-37.* https://doi.org/10.1016/j.jvolgeores.2013.06.005

Schneider, C. A., Rasband, W. S., & Eliceiri, K. W. (2012). NIH Image to ImageJ: 25 years of image analysis. *Nature methods, 9(7), 671-675.* https://doi.org/10.1038/nmeth.2089

Shea, T., Houghton, B., Gurioli, L., Cashman, K., Hammer, J. and Hobden, B. (2010). Textural studies of vesicles in volcanic rocks: An integrated methodology. *Journal of Volcanology and Geothermal Research, 190(3–4), pp. 271-289.* https://doi.org/10.1016/j.jvolgeores.2010.02.013

Soriano, C., Galindo, I., Martí, J., & Wolff, J. (2006). Conduit-vent structures and related proximal deposits in the Las Cañadas caldera, Tenerife, Canary Islands. *Bulletin of volcanology*, *69*, 217-231. https://doi.org/10.1007/s00445-006-0069-2

Sparks, S. (1978). The dynamics of bubble formation and growth in magmas: A review and analysis. *Journal of Volcanology and Geothermal Research, 3, 1-37.* https://doi.org/10.1016/0377-0273(78)90002-1

Stanton-Yonge, A., Griffith, A., Cembrano, J., Julien, R. and Iturrieta, P. (2016). Tectonic role of margin-parallel and margin-transverse faults during oblique subduction in the Southern Volcanic Zone of the Andes: Insights from Boundary Element Modeling. *Tectonics, 35(9), 1990-2013.* https://doi.org/10.1002/2016TC004226

Stasiuk, M. V., Barclay, J., Carroll, M. R., Jaupart, C., Ratté, J. C., Sparks, R. S. J., & Tait, S. R. (1996). Degassing during magma ascent in the Mule Creek vent (USA). *Bulletin of Volcanology, 58, 117-130.* https://doi.org/10.1007/s004450050130

Stern, C. (2004). Active Andean volcanism: its geologic and tectonic setting. *Revista Geológica de Chile, 31(2), 161-206.* http://dx.doi.org/10.4067/S0716-02082004000200001

Trafton, K. R., and Giachetti, T. (2022). The pivotal role of Vulcanian activity in ending the explosive phase of rhyolitic eruptions: the case of the Big Obsidian Flow eruption (Newberry Volcano, USA). *Bulletin of Volcanology, 84(12), 104.* https://doi.org/10.1007/s00445-022-01610-3

Tuffen, H., and Castro, J. M. (2009). The emplacement of an obsidian dyke through thin ice: Hrafntinnuhryggur, Krafla Iceland. *Journal of Volcanology and Geothermal Research, 185(4), 352-366*. https://doi.org/10.1016/j.jvolgeores.2008.10.021

Tuffen, H. and Dinwell, D. (2005). Fault textures in volcanic conduits: evidence for seismic trigger mechanisms during silicic eruptions. *Bulletin of Volcanology, 67, 370-387.* https://doi.org/10.1007/s00445-004-0383-5

Unwin, H., Tuffen, H., Wadsworth, F., Phillips, E., James, M., Foster, A., Kolzenburg, S., Castro, J. and Porritt, L. (2023). *Bulletin of Volcanology, 85(28).* https://doi.org/10.1007/s00445-023-01638-z

Vasseur, J., Wadsworth, F., Lavallee, Y., Hess, K. and Dingwell, D. (2013). Volcanic sintering: Timescales of viscous densification and strength recovery. *Geophysical Research Letters, 40, 5658-5664.* https://doi.org/10.1002/2013GL058105

Von Aulock, F., Kennedy, B., Schipper, C., Castro, J., Martin, D., Oze, C., Watkins, J., Wallace, P., Puskar, L., Bégué, F., Nichols, A. and Tuffen, H. (2014). Advances in Fourier transform infrared spectroscopy of natural glasses: From sample preparation to data analysis. *Lithos, 206-207, 52-64.* https://doi.org/10.1016/j.lithos.2014.07.017

Wadsworth, F., Llewellin, E., Castro, J., Tuffen, H., Schipper, I., Gardner, J., Vasseur, J., Foster, A., Damby, D., McIntosh, I., Boettcher, S., Unwin, H., Heap, M., Farquarson, J., Dingwell, D., Iacovino, K., Paisley, R., Jones, C. and Whattam, J. (2022). A reappraisal of explosive–effusive silicic eruption dynamics: syn-eruptive assembly of lava from the products of cryptic fragmentation. *Journal of Volcanology and Geothermal Research, 432, 107672.* https://doi.org/10.1016/j.jvolgeores.2022.107672

Wadsworth, F., Llewellin, E., Vasseur, J., Gardner, J. and Tuffen, H. (2020). Explosive-effusive volcanic eruption transitions caused by sintering. *Science Advances, 6, 7940.* 10.1126/sciadv.aba7940

Wadsworth, F. B., Vasseur, J., Llewellin, E. W., Schauroth, J., Dobson, K. J., Scheu, B., & Dingwell, D. B. (2016). Sintering of viscous droplets under surface tension. *Mathematical, Physical and Engineering Sciences, 472(2188), 20150780.* https://doi.org/10.1098/rspa.2015.0780

Wadsworth, F. B., Vasseur, J., von Aulock, F. W., Hess, K. U., Scheu, B., Lavallée, Y., & Dingwell, D. B. (2014). Nonisothermal viscous sintering of volcanic ash. *Journal of Geophysical Research: Solid Earth, 119(12), 8792-8804.* https://doi.org/10.1002/2014JB011453

Wilson, G., Wilson, T.M., Deligne, N. and Cole, J. (2014). Volcanic hazard impacts to critical infrastructure: A review. *Journal of Volcanology and Geothermal Research, 286, 148-182.* https://doi.org/10.1016/j.jvolgeores.2014.08.030

1101 Woods, A. W., and Koyaguchi, T. (1994). Transitions between explosive and effusive
1102 eruptions of silicic magmas. *Nature*, *370*(6491), 641-644.
1103 https://doi.org/10.1038/370641a0
1104 Wright, H., Cashman, K., Mothes, P., Hall, M., Gorki, A. and Le Pennec, J. (2012).
1105 Estimating rates of decompression from textures of erupted ash particles produced by
1106 1999–2006 eruptions of Tungurahua volcano, Ecuador. *Geology, 40(7), 619-622.*
1107 https://doi.org/10.1130/G32948.1
1108 Wysoczanski, R. and Tani, K. (2006). Spectroscopic FTIR imaging of water species in silicic
1109 volcanic glasses and melt inclusions: An example from the Izu-Bonin arc. *Journal of*
1110 *Volcanology and Geothermal Research, 156, 302–314.*
1111 https://doi.org/10.1016/j.jvolgeores.2006.03.024